A Practical Method to Determine the Five-Parameter Orientation of Intragranular Boundaries in Polycrystals

Geoffrey E. Lloyd[1*], Amicia L. Lee[1, 2] and Maren Kahl[3]

1. Institute of Geophysics and Tectonics, School of Earth and Environment, The University of Leeds, Leeds LS2 9JT, U.K.

2. Department of Geosciences, UiT Arctic University of Norway, Tromsø, 9037, Norway.

3. Institut für Geowissenschaften, Universität Heidelberg, Heidelberg, Germany

[*] **Corresponding author.**
E-mail addresses: G.E.Lloyd@leeds.ac.uk (G.E. Lloyd), amicia.lee@uit.no (A.L. Lee), Maren.Kahl@geow.uni-heidelberg.de (M. Kahl).

Abstract-Intragranular boundaries are important features of polycrystalline materials and impact on many physical and chemical properties. Knowledge of their physical orientation is often crucial to explain such properties. However, it has proved difficult to determine the complete orientation of intragranular boundaries, which involves the misorientation angle and axis about which the adjacent crystal lattices need to be rotated to bring them into coincidence and also the physical orientation of the boundary plane, expressed by the plunge and azimuth of its normal; five parameters in total. Here we present a simple and practical manual method to determine the complete intragranular boundary orientation in any crystal system. The method is developed on geometrical relationships exhibited between electron channelling patterns across a common boundary but then extended for use with electron backscattered diffraction patterns. The method recognises the channelling/diffraction band, equivalent to a crystal lattice plane, not displaced across a boundary; the boundary rotation axis must be the normal to this plane. Geometrical relationships between the boundary trace, the non-displaced band/plane and their respective plane normals constrain boundary orientation to two alternative symmetrically equivalent solutions and are evaluated via stereographic projection. The choice of solution is guided by comparison with the presence or absence of a similarly oriented band/plane observed in the original channelling/diffraction patterns. The method therefore conforms to the low-index crystallographic lattice plane and dislocation model for intragranular boundary formation and defines boundary orientation in terms of total angular misorientation due to tilt and twist components and the orientation of the boundary plane. Examples of intragranular boundary orientation determination using this method are provided in olivine. Results are compared to and differ from those obtained via conventional misorientation analysis, which only rotates adjacent crystal lattices into parallelism and does not consider boundary plane orientation. Potential extrapolation of the new method to intergranular boundaries is also considered.

1. INTRODUCTION

Intragranular boundaries are important and common features of polycrystalline materials, such as metals, ceramics and rocks. Their presence impacts critically on many physical and chemical properties, processes and behaviours, including: overall strength and failure, various types of conductivity, diffusion and creep mechanisms, recrystallisation and recovery processes, corrosion and precipitation behaviours, etc (e.g. Randle, 1993). Thus, the nature of intragranular boundaries is crucial to understanding the ultimate behaviour of polycrystalline materials. However, intragranular boundaries often exist as rather obscure elements within more detailed microstructural characterisations that focus on the properties of the regions they surround, such as the crystal texture or fabric (as defined by the crystallographic preferred orientation or CPO), subgrain size, etc. Perhaps the main reason why intragranular boundaries are often somewhat neglected is due to problems associated with defining their complete physical and/or crystallographic orientations.

On the one hand, intragranular boundaries are defects that perturb the crystallographic structure of polycrystalline materials; their definition must include recognition of this impact on the crystallography. Convention therefore recognises the misorientation angle/axis (θ/<uvw>) pair, or the crystallographic direction about which one crystal lattice must be rotated by a (minimum) angle to bring it into coincidence with an adjacent lattice. As this operation represents a pure rotation of one crystal coordinate system with respect to the other (Fig. 1a), it can be described by a rotation transformation matrix (g_m), such that,

$$\{C_i\} = g_m\{C_j\} \quad (1)$$

where $\{C_i\}$ and $\{C_j\}$ are the respective adjacent crystal coordinate systems. Misorientation angle/axis pairs comprise three degrees of freedom: the plunge/azimuth of the axis and the angle (e.g. Warrington and Bufalini, 1971; Grimmer et al., 1974; Mainprice et al., 1993; Lloyd et al., 1997; Randle, 2003). On the other hand, intragranular boundaries are also physical features (i.e. 'planes'), the orientation of which is typically crystallographically constrained but is not necessarily

crystallographically coincident. The physical orientation of the intragranular boundary plane is defined by the plunge/azimuth of the normal to the plane, which involves two degrees of freedom (Fig. 1b); however, it can also be represented crystallographically (i.e. <uvw>) with respect to one and/or other of the two adjacent crystal orientations.

Thus, the complete orientation of intragranular boundaries involves five independent parameters (e.g. Sutton and Ballufi, 1995; Kim et al., 2005; Randle, 2006; Rohrer and Randle, 2009; Ratanaphan et al., 2014; Sutton et al., 2015; Dash et al., 2017). However, whilst it is always possible to determine the misorientation angle/axis pair, particularly via electron backscattered

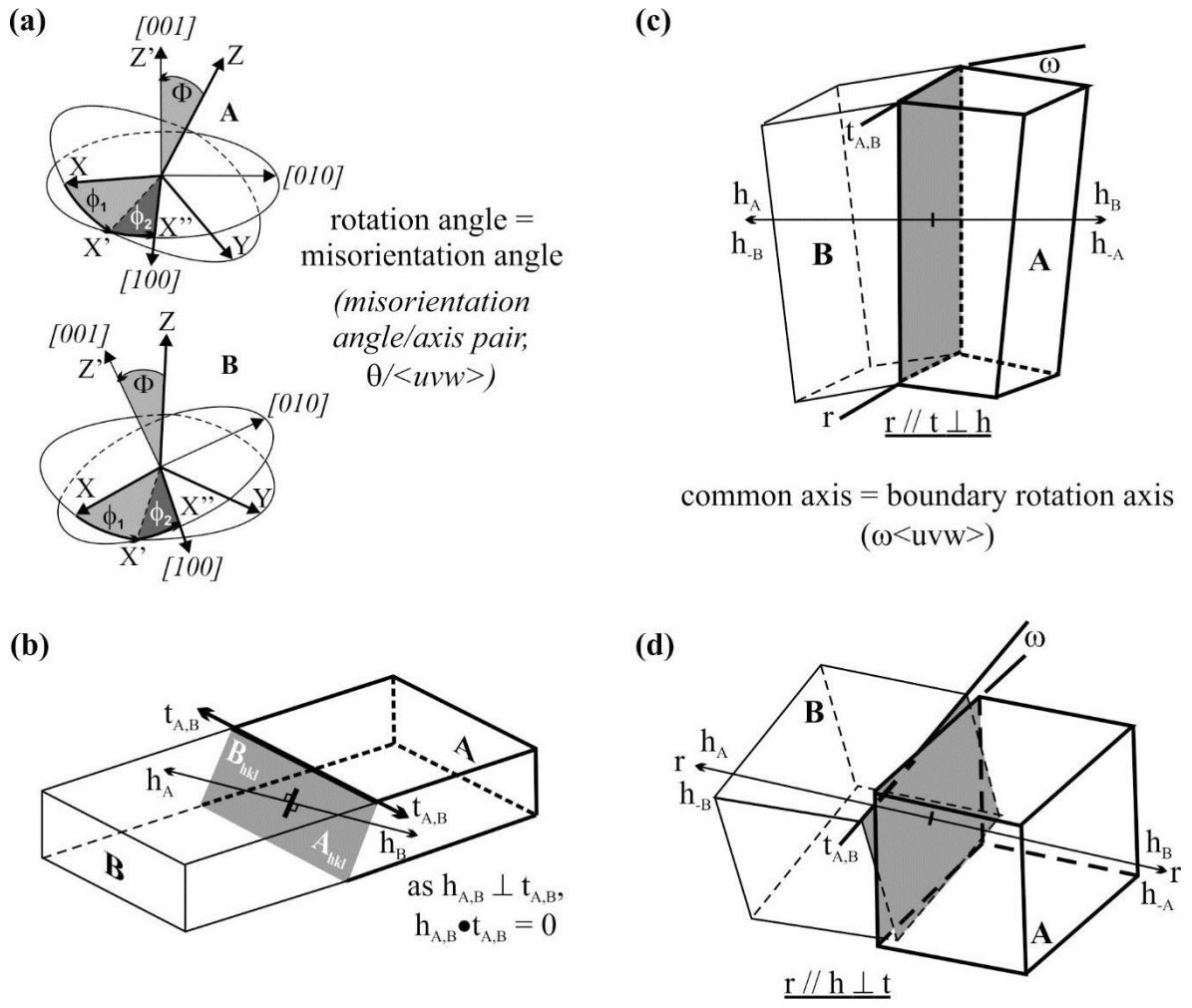

Figure 1. Intragranular boundary relationships. (a) Definition of the crystallographic orientations of two subgrains A and B and the alternative three rotations (ϕ_1, Ψ, ϕ_2) required to bring their respective lattices XYZ and X'Y'Z' into coincidence, as represented by the misorientation angle/axis pair. (b) Regions A, B share common boundary plane (A_{hkl}, B_{hkl}), trace (t) and normal (h). (c) Pure tilt boundary (r, rotation axis; ω, rotation angle). (d) Pure twist boundary.

diffraction (EBSD) in the scanning electron microscope (SEM), the direction of the boundary plane normal has proved to be notoriously difficult to establish. Although various methods, techniques and approaches do exist (e.g. optical microscopy universal stage, transmission electron microscopy, focussed ion beam, X-ray and neutron techniques, etc.), they tend to be restrictive, laborious, complex and/or expensive (e.g. Rohrer & Randle, 2009). An exception to these constraints is provided by the grain boundary character distribution (GBCD) method (e.g. Saylor et al., 2004; Rohrer et al., 2004b), which combines EBSD misorientation analysis and statistical stereology of boundary traces. However, GBCD has been reserved mostly for (cubic) metals and ceramics (e.g. Saylor et al. 2004), with only a single geological application on olivine (Marquardt et al., 2015).

More general characterisation of boundary microstructural data has recently become more common using SEM/EBSD. In part, this stems from the availability of free resource software. Perhaps the most readily available is *MTex* (e.g. Bachmann et al., 2010) and in particular its *Tilt and Twist Boundaries* script (https://mtex-toolbox.github.io/TiltAndTwistBoundaries.html). Analytical scripts based on the GBCD method for estimating the five grain boundary parameters are also available (http://mimp.materials.cmu.edu/~gr20/Grain_Boundary_Data_Archive/). In addition, an alternative but related approach using the weighted mean Burger's vector has been suggested by Wheeler et al. (2009), with a recent modification within the MTex software package (Wieser et al., 2020). However, all approaches are based a priori on the recognition of tilt and twist boundaries based on accurate definition of the misorientation axis; they do not consider either general boundaries or the orientation of the boundary plane normal. Thus, they recognise only three of the five parameters necessary to fully define an intragranular boundary.

The physical orientation of the boundary between two intragranular domains (A, B) can be described crystallographically relative to either domain (i.e. A_{hkl}, B_{hkl}; see Fig. 1b). The boundary plane can also be described by its trace ($t_{A=B}$) and normals ($h_{A,B}$) relative to either grain. As these are perpendicular,

$$h_{A,B} \cdot t_{A,B} = 0 \quad (2)$$

Within this construction, two ideal 'end-member' intragranular boundary configurations can be recognised: pure tilt (Fig. 1c) and pure twist (Fig. 1d) boundaries.

Pure tilt intragranular boundaries (Fig. 1c) develop by the progressive addition of, in principal, a single set of edge dislocations to achieve the misorientation between adjacent domains (e.g. Burgers, 1939a, b and 1940; Buranova, 1940; Shockley and Read, 1949; Read and Shockley, 1950). A rotation angle (ω) and axis (r) can therefore be recognised. As the rotation axis lies within the boundary plane and hence perpendicular to the boundary plane normal (h; Fig. 1c),

$$r \cdot h = 0 \quad (3)$$

In contrast, pure twist intragranular boundaries (Fig. 1d) develop via (at least) two sets of (not necessarily orthogonal) screw dislocations to achieve the misorientation between adjacent domains (e.g. Bragg, 1940; Burgers, 1940; Shockley and Read, 1949; Read and Shockley, 1950). In this case, the rotation axis is perpendicular to the boundary plane and hence parallel to its normal, such that,

$$r \cdot h = 1 \quad (4)$$

In practice most boundaries are probably combinations of tilt and twist components necessary to create the 'best-fit' between adjacent domains. Thus,

$$0 \text{ (pure tilt)} \leq \text{TTC} \leq 1 \text{ (pure twist)} \quad (5)$$

where TTC is the vector product of the rotation axis (r) and boundary plane normal (h) and is known as the boundary tilt-twist component index (Amouyal et al., 2005). However, and in spite of the apparent simplicity of Eqns 3 – 5, a boundary separating two adjacent misoriented crystal lattices can have an effectively infinite number of physical orientations, defined by its planar normal (Fig. 1b - d). Herein lies the inherent problem and concomitant requirement for defining the complete five-parameter orientation of intragranular boundaries.

In this contribution, we propose a simple practical solution for the definition of the five-parameter

116 orientation of intragranular boundaries. Our solution arises from the recognition that all
117 intragranular boundaries involve four common geometrical parameters (Fig. 1): boundary trace (t),
118 boundary plane normal (h), rotation axis (r) and rotation angle (ω). In addition, the basic
119 requirement involves knowledge of the crystallographic orientation of the domains on either side of
120 a boundary, as well as the (crystallographic) orientation of the boundary plane normal direction.
121 Whilst we derive our solution from original observations made via SEM back-scattered electron
122 (BSE) electron channelling (EC), we subsequently demonstrate not only how it can be adapted for
123 EBSD data but also suggest how it may be extended to (some) intergranular boundaries.

124 ## 2. METHOD

125 ### 2.1 Electron channelling

126 SEM/EC (e.g. Hirsch et al., 1962; Venables and Harland, 1973; Joy, 1974; Goldstein and Yakowitz,
127 1975; Joy et al., 1982) is a related technique to SEM/EBSD (e.g. Dingley, 1989; Prior et al. 1999
128 and 2009) for determining crystallographic orientations via electron channelling patterns (ECP)
129 rather than EBSD patterns. It also provides images based on sample crystallographic microstructure
130 via BSE 'orientation contrast' (OC), also known as electron or orientation channelling contrast
131 imaging (ECCI/OCCI) in recent literature (e.g. Zaefferer and Elhami, 2014); such images (e.g. Fig.
132 2a) are equivalent to EBSD fore-scattered electron (FSE) images. The principal differences between
133 EC and EBSD patterns are as follows.

134 (1) In EBSD, a vertical electron beam strikes a sample tilted at ~65-70°, whereas for EC a vertical
135 electron beam is rocked about a fixed point on a horizontal sample. (2) The angular spread of
136 patterns can approach ~100° in EBSD (Fig. 2b, c) but is typically only up to ~24° in EC (Fig. 2d, e),
137 as determined by the rocking angle (±RA) of the incident electron beam; it is much easier therefore
138 to identify (index) EBSD patterns, particularly via automation and in phases with low crystal
139 symmetry. (3) However, the smaller angular spread for ECP results in better angular resolution

compared with EBSD patterns (Fig. 2b-e). (4) In contrast, the maximum spatial resolution of ECP formation is from 1 - 10μm due to aberrations in the SEM objective lens, which is at least an order of magnitude greater than conventional EBSD. (5) Because ECPs are produced by rocking a stationary electron beam about a point on the sample surface, a one-to-one relationship is

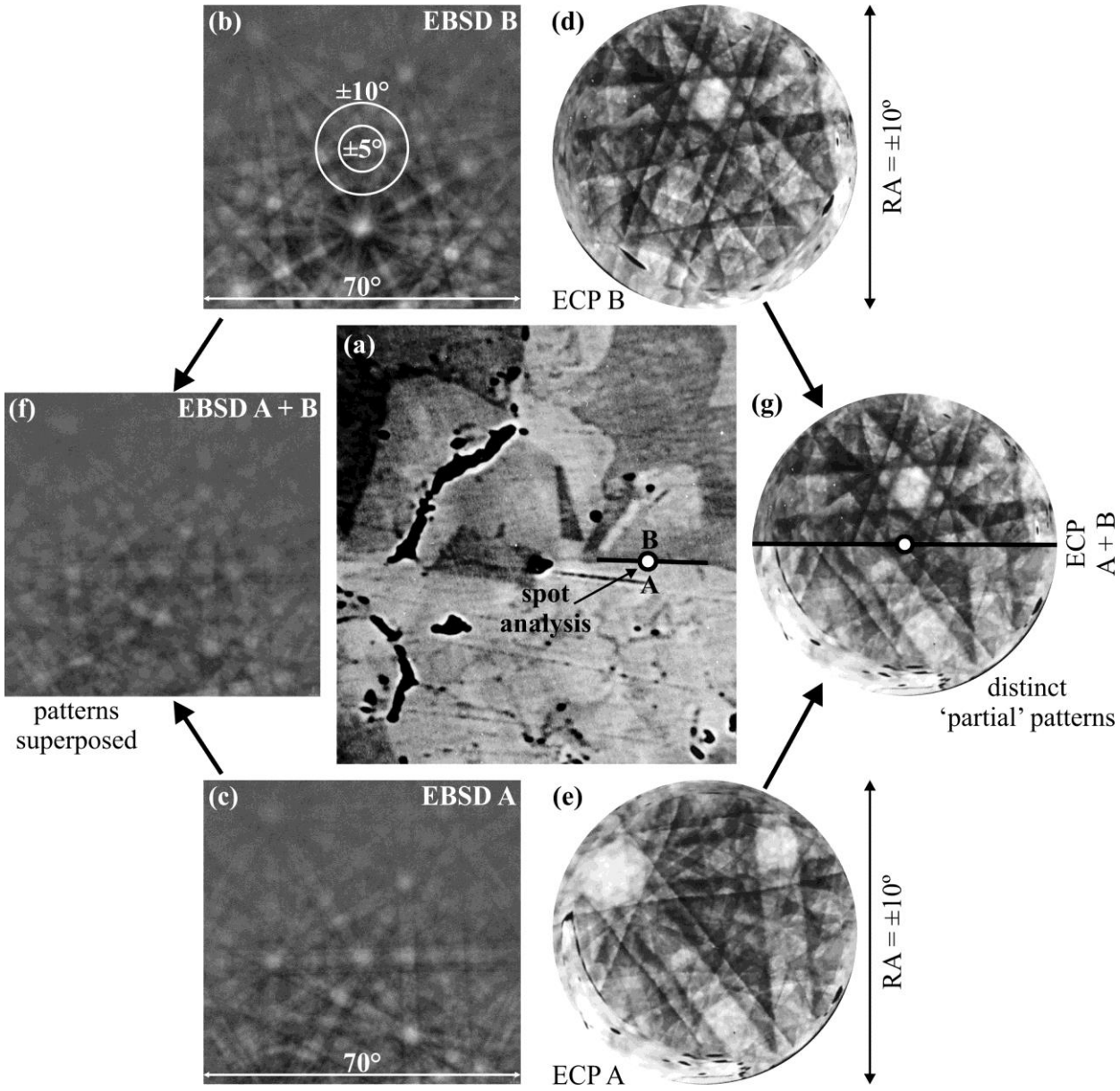

Figure 2. Comparison between electron backscattered diffraction (EBSD, left) and electron channelling (EC, right) patterns from pyrite. (a) EC orientation contrast (OC) and/or EBSD fore-scattered electron (FSE) image; note adjacent regions A and B separated by a distinct boundary. (b) and (c) Individual EBSD patterns from regions B and A respectively cover ~70° of the crystal structure. (d) and (e) Individual EC patterns (ECP) from regions B and A respectively cover only ~20° (i.e. electron beam 'rocking angle', RA, = ±10°) of the crystal structure. (f) The EBSD pattern from the boundary between A and B is formed by the complete superposition of patterns (b) and (c), resulting in an indistinct image. (g) The ECP from the boundary between A and B is composed of the relevant halves of patterns (d) and (e), resulting in a distinct image consisting of recognisable 'partial' patterns.

maintained between each point on the surface and in the pattern such that 'partial' ECPs characteristic of the crystallographic orientation on each side of a boundary are produced (Fig. 2g); this one-to-one relationship does not exist for EBSD patterns, which instead are superposed and appear indistinct (Fig. 2f). It is this last characteristic that provides the crucial opportunity to determine the complete orientation of intragranular boundaries.

2.2 Boundary rotation angle(s) and axis

Figure 3a is a schematic representation of partial ECP configurations across an intragranular boundary (trace t and trace normal h_t) and illustrates how the boundary tilt angle (ω) and axis (r) can be determined. The crucial observation is to recognise the EC (diffraction) band (or crystal lattice plane) that is not displaced across the boundary trace. This band 'dips' towards the pattern centre by 90-β°. The value of β is determined via the internal scaling present in ECP formation, which is constrained by the specific SEM operating conditions (i.e. accelerating voltage, working distance, etc.) and indicated by RA (degrees/radians) and the pattern diameter (D mm), such that,

$$\beta° = Bmm \times 2RA°/Dmm \quad (6a)$$

where Bmm is the orthogonal linear distance measured in the ECP between the non-displaced channelling band and the pattern centre (Fig. 3a). Similar calculations can be defined for all other EC bands and angular distances.

For the EC band to be non-displaced, the displacement translation vector (d_v) must be contained within the band (Fig. 3b). Thus, the normal to the non-displaced EC band must be parallel to the boundary rotation axis. As well as the non-displaced EC band, any bands parallel to the boundary trace are also recognised. The ECP configuration prior to boundary formation can be restored by translating one partial pattern relative to the other, parallel to the displacement translation vector of the non-displaced EC band until all bands become aligned (Fig. 3b). The boundary rotation angle (ω_r) is then obtained from the displacement distance (d) in a similar manner to Eqn 6a,

$$\omega_r° = dmm \times 2RA°/Dmm \quad (6b)$$

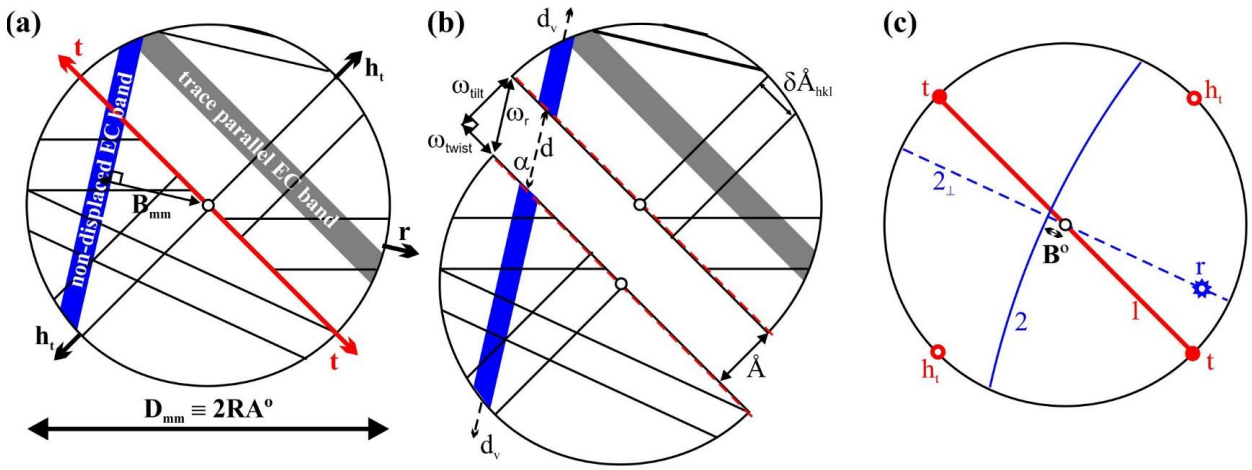

Figure 3. Determination of boundary rotation axis and angles. (a) Schematic partial ECPs across an intragranular boundary (t, trace; h_t, trace normal). The normal to the non-displaced EC band, which 'dips' 90-β° where β = BxD/2RA (B, linear distance from non-displaced band centre to pattern centre; D, twice the rocking angle), defines the direction of the boundary rotation axis (r). Note also a boundary trace parallel EC band. (b) Restoration of pre-boundary formation ECP configuration via the displacement vector (d_v) parallel to the non-displaced EC band (α, acute angle between non-displaced band and boundary trace). Total rotation angle (ω_r) is parallel to the displacement distance (d), with tilt (ω_{tilt}) and twist (ω_{twist}) components normal and parallel to the boundary trace (determined via internal scaling relative to RA and D); the tilt component can also be represented in terms of distance (Å) via internal scaling provided by EC bandwidth ($\delta Å_{hkl}$). (c) Upper hemisphere stereographic (Wulff/equal angle) and/or crystallographic projection representation: 1, boundary trace (t); 2, non-displaced EC band; $2_\perp$, vertical plane normal to non-displaced EC band; r, boundary rotation axis.

In the example shown in Fig. 3, the displacement vector is oblique to the boundary trace, which indicates a general boundary. From Fig. 1, pure tilt displacements develop normal to the boundary trace via rotation parallel to the trace, whereas pure twist displacements develop parallel to the trace via rotation normal to it. The tilt (ω_{tilt}) and twist (ω_{twist}) angular components of a general boundary can therefore be determined by resolving ω_r into its boundary trace normal and parallel displacements respectively,

$$\omega_{tilt}° = d\sin\alpha\ 2RA°/Dmm \quad (6c)$$

$$\omega_{twist}° = d\cos\alpha\ 2RA°/Dmm \quad (6d)$$

where α is the (acute) angle between the non-displaced EC band and the boundary trace (t).

The displacement normal to the boundary trace can also be expressed as a length (e.g. in angstroms, Å) via the scaling provided by the width of the diffraction bands, which depends on the SEM

accelerating voltage used, and is readily available in EC/EBSD processing software. Figure 3c summarises the boundary trace (1), non-displaced EC band (2), including its vertical normal plane ($2_{\perp}$), and rotation axis (r) orientations in terms of (Wulff/equal angle) stereographic and/or crystallographic projections.

2.3 Boundary plane orientation

As stated previously, the main problem with defining the complete five-parameter orientation of intragranular boundaries concerns the physical orientation of the boundary plane normal direction. This is not a problem unique to intragranular boundaries. For example, the inclination (ψ) of boundaries formed during grain boundary sliding (gbs) can be determined from a relatively simple relationship between the offsets of three mutually perpendicular directions (u, v, w) and the angle (θ) between the trace of the boundary and a reference direction, such that (Langdon, 2006),

$$\tan\psi = (u - w\tan\theta)/v \qquad (7)$$

However, it is impractical to use this equation (e.g. in the determination of the contribution of gbs to the total strain) because of the difficulties of measuring the angles θ and ψ at every boundary (Langdon, 2006; Mohamed, 2011). Similarly, the movement characteristics of geological faults relies implicitly on knowledge of the dip of the fault plane (e.g. Redmond, 1972; Yamada and Sakaguchi, 1995 Xu et al., 2007 and 2009; Lisle and Walker, 2013); if the dip is not known, it is difficult to determine from other parameters except for specific combinations (e.g. Nieto-Fuentes et al., 2014). Fortunately, the geometry of partial ECPs formed across a common intragranular boundary (e.g. Fig. 3) offers a relatively simple practical solution to the problem.

The solution assumes implicitly that intragranular boundary orientations are constrained not only crystallographically to low-index lattice planes (i.e. Read and Shockley, 1950) but also by the origin of ECPs. Following Friedel's rule (Friedel, 1913), which introduces an effective centre of symmetry, each EC band originates from the centre of a spherical projection directly below the pattern centre defined by the rocking position (Fig. 4a). Thus, only bands 'steeper' than (90 - RA)°

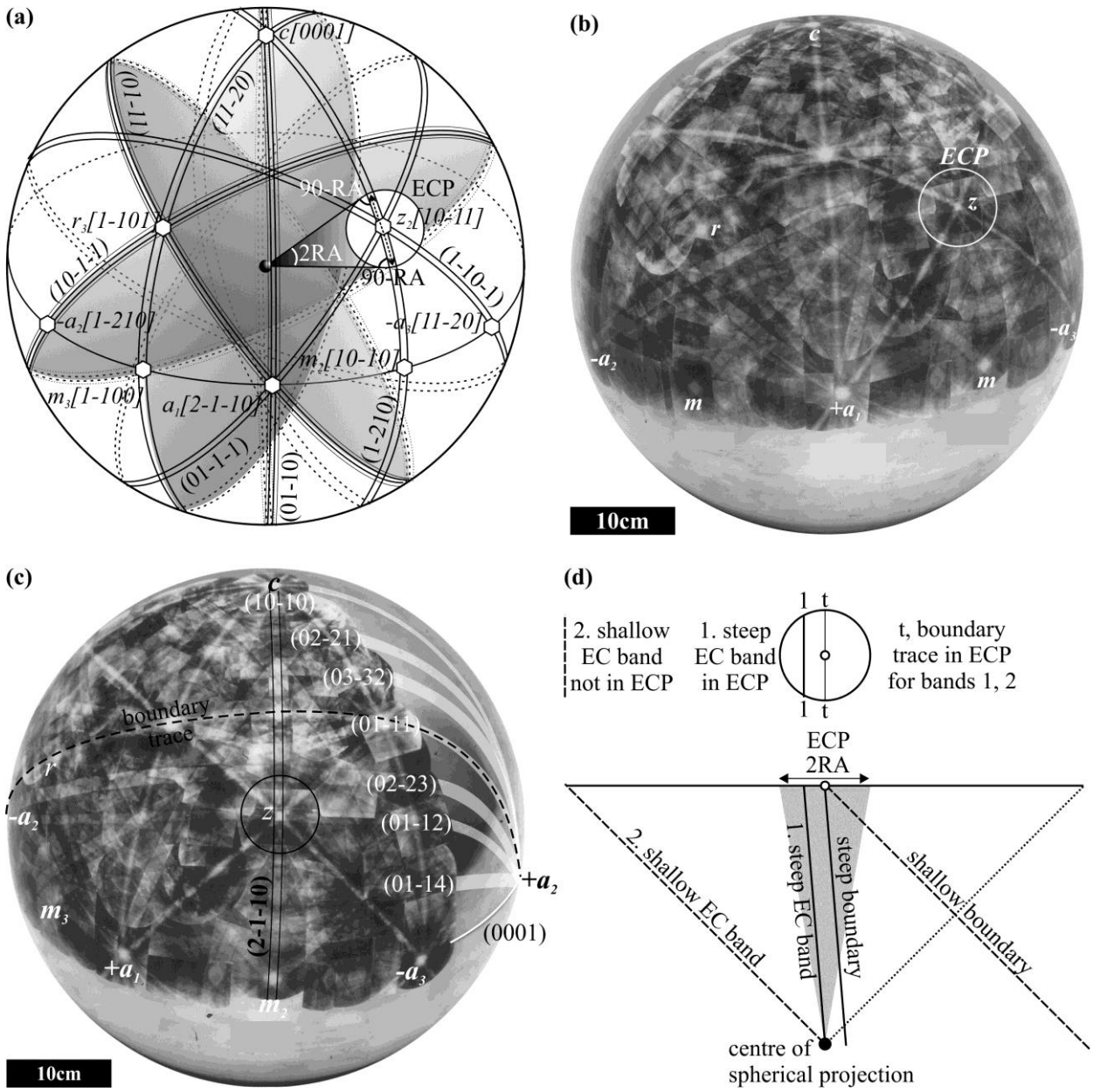

Figure 4. EC spherical projection. (a) Schematic representation of trigonal α-quartz three-dimensional crystallography and ECP formation on the projection surface. (b) Quartz EC crystallographic unit triangle constructed via photo-montage over a spherical surface (Lloyd and Ferguson, 1986). (c) Multiple possible boundary plane parallel low-index lattice planes, all of which intersect at $\pm a_2$ for a boundary plane trace normal to (2-1-10) and apparently parallel to and coincident with (01-11). (d) Schematic representation of parallelism but not coincidence between boundary trace (t) and EC bands (in)visible in an ECP.

are visible in any ECP. As all bands are inclined towards the centre of the pattern, the angle of projection is given by Eqn 6a. The construction shown in Fig. 4a led directly to the early use of spherical ECP maps for crystallographic indexing purposes (e.g. Fig. 4b; Lloyd, 1987) and ultimately to (interactive) spherical Kikuchi maps (e.g. Day 2008 and 2009; Zhu et al., 2019; Hielscher et al. 2019), which we make use of later in this contribution.

The crux of our solution is that for intragranular boundaries constrained crystallographically to low-index lattice planes, the trace of the boundary plane is parallel to an EC band ideally present in the (partial) ECPs (e.g. Fig. 3a). However, as shown in Fig. 4c, there can be multiple possible solutions. The problem therefore is to determine which specific lattice plane is parallel to the boundary plane. In fact, the problem is even more complex as the boundary plane, although constrained to be parallel to a low-index lattice plane, does not have to be coincident with that plane (e.g. Fig. 3a). This is because all EC bands originate from the centre of a spherical projection (Fig. 4a), such that the distance between the band and the centre of the ECP increases with inclination (Fig. 4c). In contrast, intragranular boundaries are physical features that do not originate from the centre of the spherical projection. Thus, whilst EC bands dipping $<(90 - RA)°$ do not appear in the ECP, a mutually parallel intragranular boundary plane can still be observed in the image. Concomitantly, it follows that straight boundary traces, including those through the centre of ECPs, are not constrained to be vertical. The solution to the problem of determining the physical orientation of intragranular boundaries is provided by stereographic projection analysis based on the geometry of partial ECPs. Figure 3c shows the basic relationships between the boundary trace and its vertical normal plane, the non-displaced EC band and its vertical normal plane, and the boundary rotation axis plotted in (Wulff/equal angle) stereographic and/or crystallographic projections. We now develop this construction in Fig. 5.

We first plot (Fig. 5a) the boundary trace (1), the non-displaced EC band (2) and their respective vertical normal planes ($1_{\perp}$, $2_{\perp}$). The intersection (3) of the non-displaced EC band (2) and the vertical section plane normal ($1_{\perp}$) defines the pitch of the former on the latter. Next (Fig. 5b), we construct small circles (4) with radii equal to the pitch (3) centred on the strikes (t) of the boundary trace (1); these small circles define the loci of pitches of the boundary plane relative to the trace (t). The intersections (5) of the small circles (4) with the vertical section plane normal to the non-displaced EC band ($2_{\perp}$) define the pitches of the boundary plane on that plane. The strikes (t) of the boundary trace (1) and the small circle intersections (5) must lie in the boundary plane; the great

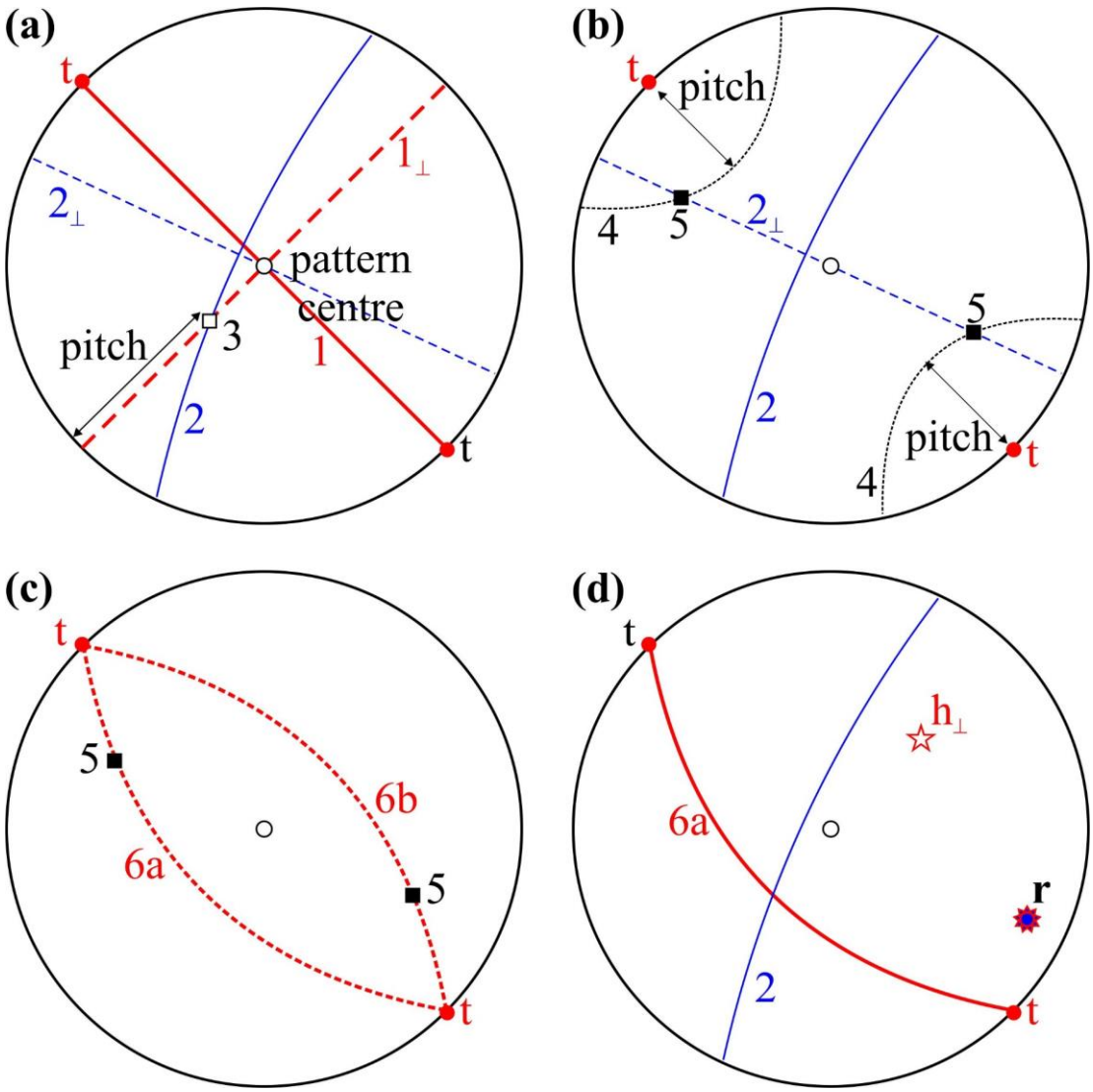

Figure 5. Determination of boundary plane orientation: red and blue colours indicate boundary plane and non-displaced EC band related elements respectively (see Fig. 3). (a) Plot of boundary trace (1), non-displaced EC band (2) and their respective vertical normal planes ($1_\perp$, $2_\perp$); intersection (3) of 2 and vertical $1_\perp$ defines the pitch of the former on the latter. (b) Small circles (4) with radii equal to the pitch (3) constructed about strikes (t) of the boundary trace (1); the small circles define the loci of the pitches of the boundary plane and their intersections (5) with the vertical section plane normal to the non-displaced EC band ($2_\perp$) define the pitches of the boundary plane on that plane. (c) Strikes (t) of boundary trace (1) and small circle intersections (5) must lie in the boundary plane, such that great circles (6a, b) through these points define its potential orientations; the most likely alternative is determined by coincidence between the planes and any EC band in the partial ECPs (e.g. Fig. 3a). (d) Determination of non-displaced EC band normal (r, boundary rotation axis) and boundary plane normal ($h_\perp$) directions.

circles (6a, b) through these points therefore define its two alternative orientations (Fig. 5c). To choose the most likely alternative, we check for coincidence between the predicted boundary planes and any low-index boundary-parallel EC band (e.g. Fig. 3a); we show below that this identification is facilitated by spherical Kikuchi maps (SKM). Finally (Fig. 5d), the non-displaced EC band

normal (r), which defines the boundary plane rotation axis, and boundary plane normal ($h_{\perp}$) directions are plotted. The crystal indices of these positions, $[uvw]_r$ and $[uvw]_{h\perp}$, are the values that should be used in Eqn. 4 to calculate the TTC component of the boundary.

In the next section, we provide actual examples of the application of the method to intragranular boundaries in olivine. The examples were imaged at the University of Leeds using a Tescan Vega3 SEM operated in EC mode using a 25kV accelerating voltage, a specimen working distance of 9mm and rocking angles of ±10-11°; beam currents were varied to obtain the best OC and ECP images.

3. EXAMPLE RESULTS

Figure 6a is an EC orientation contrast image of a single forsteritic olivine (orthorhombic, space group Pbnm) grain from a sample of volcanic ejecta (Kahl et al., in prep.); note the intragranular boundary comprising long, straight and short, kinked segments. Also shown are ECPs (1 and 2) from each side of the boundary (Fig. 6b, c). Whilst the patterns are slightly different due to the misorientation introduced by the boundary (e.g. compare their respective Euler angle triplets), their individual configurations are consistent along each side of the boundary irrespective of the (boundary) segment orientation. Figures 6d and e show partial ECPs from each side (1 and 2) of the two boundary segments respectively, obtained by rocking the incident electron beam on the boundary as indicated. The boundary traces are clearly observed in both images by displacement of EC bands. The displacement sense is either sinistral or dextral depending on the orientation (i.e. angle of intersection) of the EC band relative to the boundary trace. However, one EC band towards the upper left, which is the same for both boundary segments, is continuous across the boundary.

Spherical geometry dictates that the inclination ('dip') of any EC band is the (angular) distance between the normal to the band, measured from the band centre, and the centre of the pattern subtracted from 90º (Eqn 6). All bands 'dip' towards the pattern centre (i.e. the centre of the

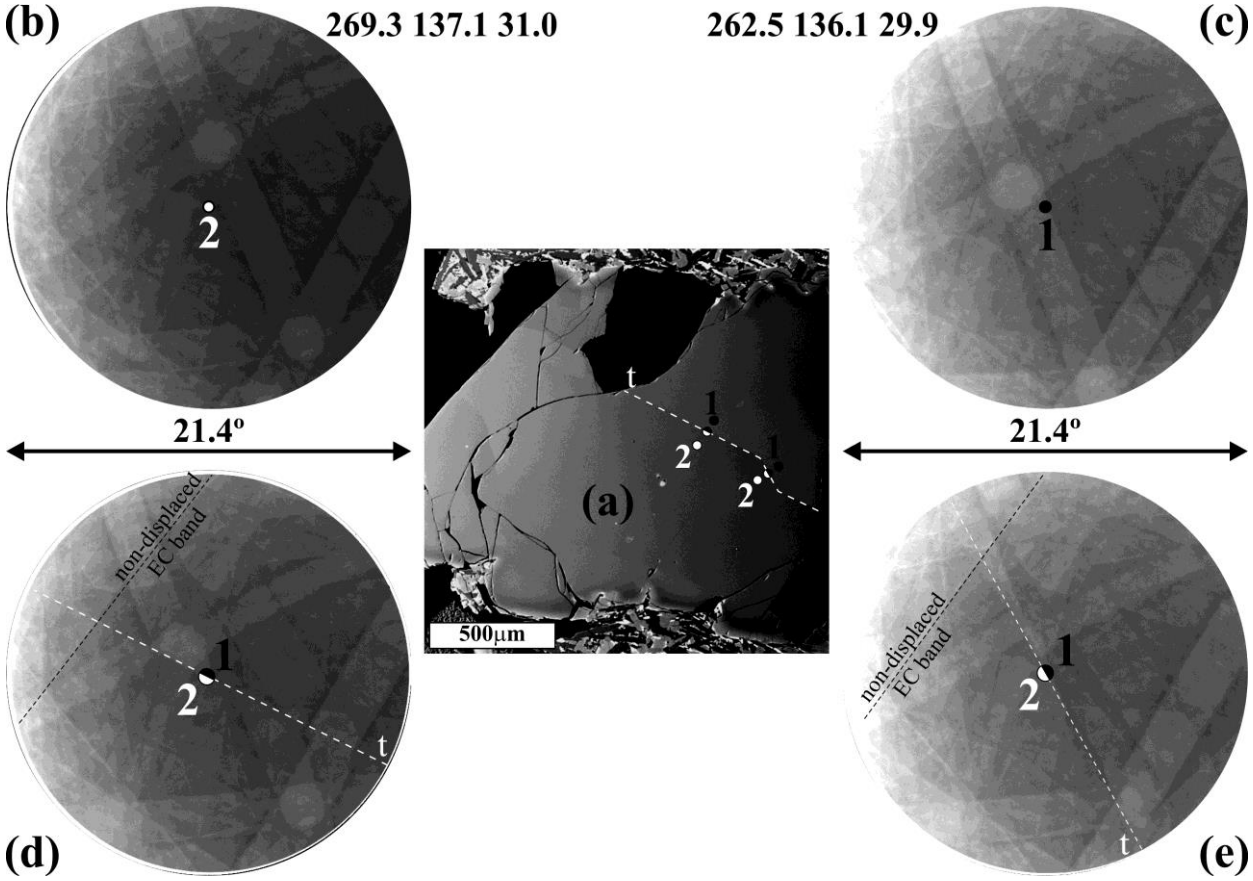

Figure 6. Intragranular boundary orientation method example. (a) Olivine grain with intragranular boundary comprising long, straight and short, kinked segments (electron channelling orientation contrast). (b) and (c) Complete electron channelling patterns from points 1 and 2 either side of the boundary (note Euler angle triplets); the patterns and hence orientations do not change along the boundary segments. (d) and (e) Partial electron channelling patterns from the long, straight (d) and short, kinked (e) boundary segments (broken white lines); note displacement of all channelling bands except for one, which is the same for both segments.

spherical projection, which is therefore upper hemisphere). Scaling is provided by the rocking angle involved in pattern formation, which is RA = ±10.7º for this example.

3.1 Boundary rotation angles and axes

The rotation angles and axes for the two olivine intragranular boundary segments (Fig. 6) are determined following the procedure outlined above (Fig. 3), illustrated in Figs 7a, b and 8a, b. Based on the orthogonal distances from the centres of the non-displaced band to the rocking positions (i.e. pattern centres), it is inclined at 81.8° and 82.2° towards the pattern centres respectively for the two segments. As the normal to the non-displaced EC band defines the orientation of the boundary plane rotation axis, this must be the same crystallographically for both

boundary segments irrespective of the different orientations of their boundary traces and hence planes. The rotation axes for the two segments therefore plunge 8.2° and 7.8° respectively normal to the non-displaced band.

The rotation angles associated with formation of the two intragranular boundary segments can be determined by translating one of the partial patterns parallel to the non-displaced EC band until all of the other EC bands become continuous (Figs 7b and 8b). In other words, the effect of the intragranular boundary has been 'removed'. In the examples shown, the translation directions are not orthogonal to the trace of either boundary segment, indicating that both segments are general boundaries and that the overall rotation angle (ω) comprises both tilt (ω_{tilt}) and twist (ω_{twist}) components.

The overall rotation angle is defined by the (angular) separation of the partial patterns along the displacement vectors, according to the internal scaling present in the ECPs (i.e. RA = ±10.7°) and using Eqn 6. The tilt and twist components are the displacements respectively normal and parallel to the boundary trace such that,

$$\omega = (\omega_{tilt}^2 + \omega_{twist}^2)^{1/2} \quad (8)$$

In terms of the long, straight segment, ω = 3.3°, with ω_{tilt} = 3.1° and ω_{twist} = 1.0° (Fig. 7b); whilst for the short, kinked segment, ω = 2.6°, with ω_{tilt} = 2.2° and ω_{twist} = 1.4° (Fig. 8b). As recognised previously, both segments are general boundaries. However, by comparing the relative values of the tilt and twist components for each segment, the long, straight segment involves significantly more tilt than twist in its configuration. To quantify the boundary segments more precisely (e.g. by the TTC index) requires accurate definition of their boundary plane orientations.

3.2 Boundary plane orientations

To determine the orientation of the two boundary plane segments (Fig. 6a), we follow the workflow outlined in Fig. 5. First, we plot (Figs 7c and 8c) Wulff/equal angle upper hemisphere stereographic

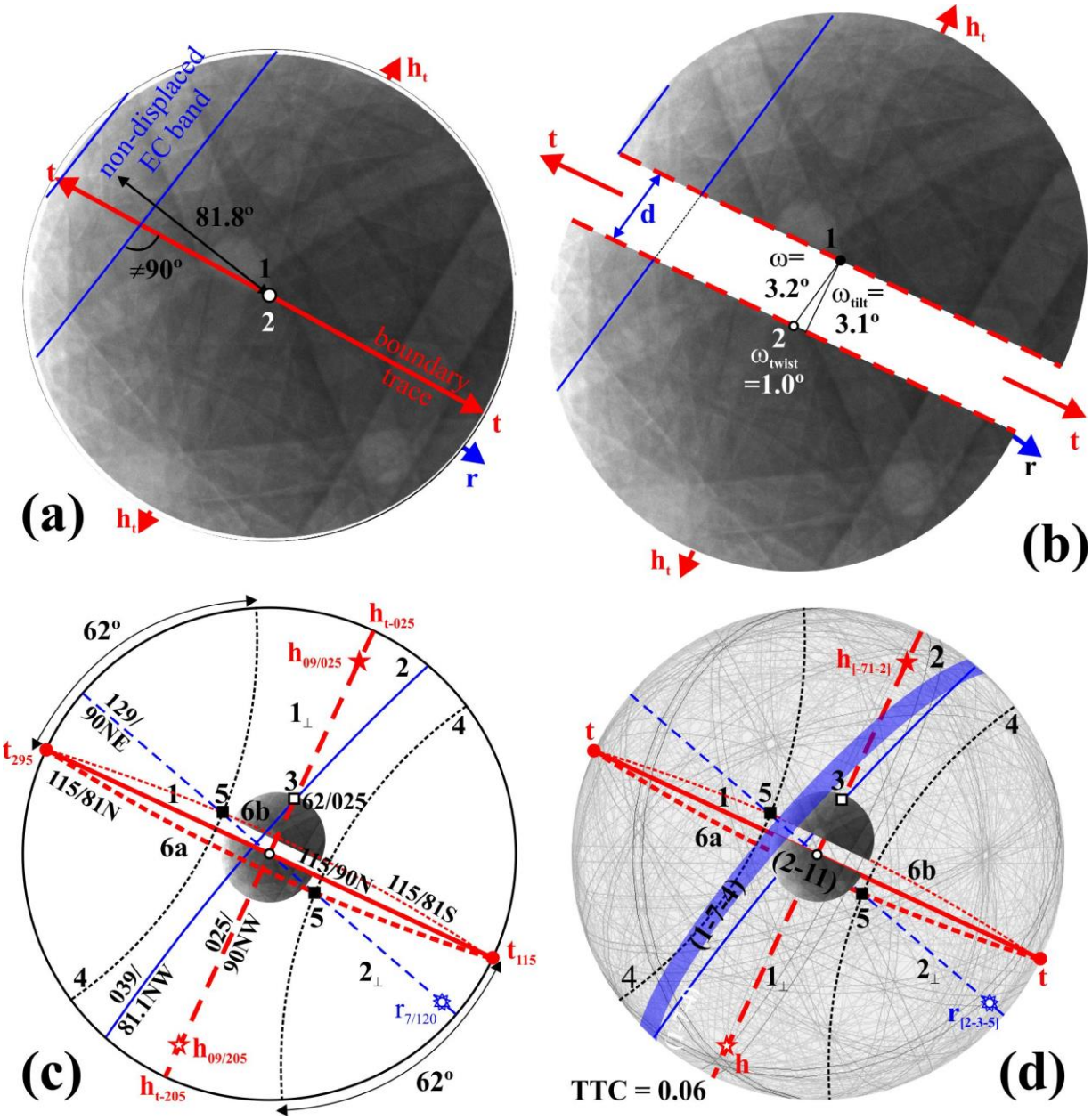

Figure 7. Intragranular boundary orientation determination: olivine long, straight segment (see Fig. 6). Nomenclature and colours as in Figs 3 and 5. (a) Partial ECPs from across the boundary segment (t, trend and h_t, trend normal); all EC bands are displaced across the boundary except one (indicated, with 'strike/dip/sense'); normal to this band defines boundary rotation axis (r, 09/129 'plunge/azimuth'). (b) Partial ECPs 'restored' to pre-boundary formation positions by translation parallel to non-displaced EC band such that all bands are continuous. The translation distance is the boundary rotation angle (ω), which can be resolved into its boundary normal tilt (ω_{tilt}) and boundary parallel twist (ω_{twist}) components for general boundaries. (c) Stereographic projection (*upper* hemisphere, Wulff/equal angle) of progressive steps involved in boundary orientation determination (see Fig. 5 and associated text for definition of numbers/symbols). Two symmetrical solutions are indicated, both 'striking' 115° and 'dipping' either 81°N or 81°S. (d) Spherical Kikuchi map (SKM) representation illustrating crystallographic indexing procedure and final selection of boundary plane orientation (115/81N) based on coincidence with (2-11) EC band/lattice plane. Note also crystallographic orientations of r and h (i.e. true boundary plane normal), allowing determination of TTC = 0.17, close to a pure tilt intragranular boundary.

296

297 projections of the orientations of the boundary trace (1), its (vertical) normal plane ($1_{\perp}$), the non-
298 displaced EC band (2) and its (vertical) normal plane ($2_{\perp}$). The values are determined using Eqn 6
299 (0 - 90°) and the clockwise azimuthal direction around the pattern circumference (0 – 180°). Next,
300 we determine the intersection (3) of the non-displaced EC band on the (vertical) normal to the
301 boundary segment trend; the intersection defines the loci of the pitches of the boundary plane as
302 small circles (4) about the strike (t) of the boundary trace (1). The intersections (5) of the small
303 circles (4) with the vertical section plane normal to the non-displaced EC band ($2_{\perp}$) define the
304 pitches of the boundary plane on that plane. The strikes (t) of the boundary trace (1) and the
305 intersections (5) must lie in the boundary plane; great circles through these points therefore define
306 its potential orientations (6).

307 Typically, two alternative and symmetrical grain boundary plane solutions are obtained (6a and 6b).
308 To choose the most likely alternative, we check for coincidence between the predicted boundary
309 plane orientations and an EC band by overlaying the partial ECPs onto the stereographic projection
310 (Figs 7c and 8c). This is because the dislocation model for intragranular boundary formation
311 predicts that they coincide with low index crystal planes. For the long, straight segment, alternative
312 6a oriented 115°/81°N is coincident with an EC band that is parallel to the boundary trace (see Figs
313 6b-d and 7a, b), which is therefore selected. For the short, kinked segment, alternative 6a oriented
314 158°/83°W is also coincident with an EC band that is parallel to the boundary trace (see Figs 6b-d
315 and 8a, b), which is therefore selected. Having selected the appropriate boundary plane orientations,
316 the boundary plane normal directions ($h_{\perp}$) can be determined for both segments.

317 Figures 7c and 8c define the boundary segment orientations in terms of spherical angles. As such,
318 they are measured and represented in terms of the sample coordinate system. In this example, the
319 olivine grain is from a sample of volcanic ejecta and consequently has no specific specimen
320 orientation. It would be useful therefore to express the boundary segment plane orientations in
321 terms of (olivine) crystallography. This is possible by use of spherical Kikuchi maps (SKM; see

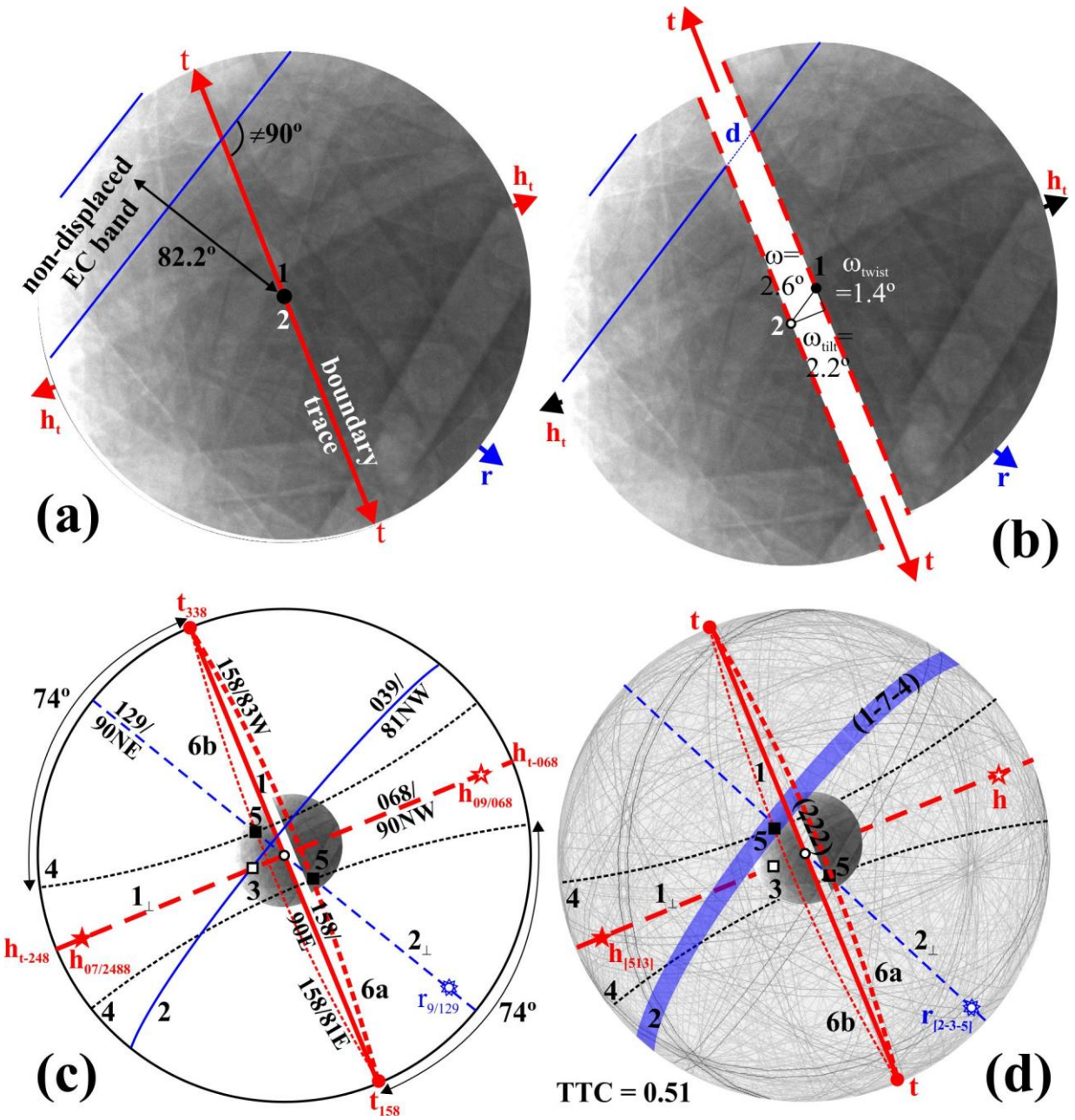

Figure 8. Intragranular boundary orientation determination: olivine short, kinked segment (see Fig. 6). Nomenclature and colours as in Figs 3 and 5. (a) Partial ECPs across each boundary segment (t, trend and h_t, trend normal); all EC bands are displaced across the boundary except for one (indicated, with 'strike/dip/sense'); normal to this band defines boundary rotation axis (r, 09/129 'plunge/azimuth'). (b) Partial ECPs 'restored' to their pre-boundary formation positions by translation parallel to the non-displaced EC band such that all bands are continuous. The translation distance is the boundary rotation angle (ω), which can be resolved into its boundary normal tilt (ω_{tilt}) and boundary parallel twist (ω_{twist}) components for general boundaries. (c) Stereographic projection (*upper* hemisphere, Wulff/equal angle) of progressive steps involved in boundary orientation determination (see Fig. 5 and associated text for definition of numbers/symbols). Two solutions are indicated, both 'striking' 158° and 'dipping' either 83°W or 81°E. (d) Spherical Kikuchi map (SKM) representation illustrating crystallographic indexing procedure and final selection of boundary plane orientation (158/83W) based on coincidence with (222) EC band/lattice plane. Note also crystallographic orientations of r and h (i.e. true boundary plane normal), allowing determination of TTC = 0.45, indicating a general intragranular boundary.

Day 2008 and 2009) and in particular the interactive versions for olivine available in the HKL Channel5 and/or AZtecCrystal software packages (Fig 7d and 8d). In effect, the stereographic projection construction is simply overlain onto an SKM defined by the orientation of the ECPs, either via visual comparison or, more accurately, via their Euler angle triplets (e.g. Figs 6a, b); however, care is required beyond 45° from the centre of projection due to increasing spherical distortion. It is also possible to incorporate the 'restored' partial ECPs into the construction (Figs 7d and 8d). The interactive nature of the SKM then makes it a simple matter to index crystallographically the relevant planes and direction.

Based on the olivine SKM, the non-displaced EC band common to both boundary segments is the $(1\bar{7}\bar{4})$ lattice plane (Figs 7d and 8d). The long, straight boundary segment is parallel to the $(2\bar{1}1)$ lattice plane, whilst the short, kinked boundary segment is parallel to the (222) lattice plane. However, a problem arises in the determination of the normal directions to these lattice planes due to non-cubic (i.e. orthorhombic) symmetry relationships. We resort therefore to relationships involving the reciprocal (orthorhombic) crystal lattice and metric tensor (e.g. Bond, 1976; Boisen and Gibbs, 1990; De Graf and McHenry, 2012),

$$M^* = \begin{bmatrix} a*^2 & 0 & 0 \\ 0 & b*^2 & 0 \\ 0 & 0 & c*^2 \end{bmatrix} \quad (9)$$

where a* = bc/V, b* = ac/V and c*=ab/V; a = 4.76Å, b = 10.21Å and c = 5.98Å are the orthogonal olivine lattice parameters; and V = abc is the volume of the olivine unit cell (290.38Å^3). The direction [uvw] normal to the plane (hkl) is then given by,

$$\begin{bmatrix} u \\ v \\ w \end{bmatrix} = M^* \begin{pmatrix} h \\ k \\ l \end{pmatrix} \quad (10)$$

Thus, the rotation axis normal to the $(1\bar{7}\bar{4})$ non-displaced lattice plane is parallel to $[2\bar{3}\bar{5}]$, whilst the normal directions to the $(2\bar{1}1)$ and (222) boundary parallel lattice planes are parallel to $[7\bar{1}2]$ and [513] respectively. Combining the common rotation axis with the boundary plane normal

Table 1. Summary of olivine boundary parameters (Figs. 6 - 8)		
Boundary Parameter	**long, straight segment**	**short, kinked segment**
non-displaced EC band	$(1\bar{7}\bar{4})$	$(1\bar{7}\bar{4})$
rotation axis plunge/trend	08°/129°	08°/129°
rotation axis (r)	$\mathbf{[2\bar{3}\bar{5}]}$	$\mathbf{[2\bar{3}\bar{5}]}$
boundary plane	$(2\bar{1}1)$	**(222)**
boundary trend (t)	115°/295°	158°/328°
boundary plane normal plunge/trend	09°/025° or 205°	10/068° or 248°
boundary plane normal (h)	$[\mathbf{7\bar{1}2}]$	**[513]**
rotation angle (ω)	**3.3°**	**2.6°**
tilt component (ω_{tilt})	*3.1°*	*2.2°*
twist component (ω_{twist})	*1.0°*	*1.4°*
tilt-twist component (TTC)	0.17	0.45
'excess volume' nm	25.16	8.87
numbers in bold represent five-parameter definition of intragranular boundary orientations		

directions yield TTC values of 0.17 for the long, straight boundary segment and 0.45 for the short, kinked boundary segment. The former is defined as close to a pure tilt boundary whilst the latter is a general boundary.

3.3 Summary

Table 1 summarises the results of the olivine intragranular boundary analyses (Figs 6 – 8) in terms of both the sample (i.e. stereographic projection plane and normal orientations) and crystallographic (i.e. crystal planes and normals) coordinate systems. The former is not representative for this example as the sample does not possess a rigorous spatial orientation as it is a sample of volcanic ejecta; however, this representation may be useful in samples that are kinematically constrained. The latter represents the complete five-parameter determination of boundary plane orientations and is constrained by the orthorhombic crystal structure of olivine. For example, the crystallographic orientations can be represented in terms of conventional upper and/or lower hemisphere orthorhombic projections (Fig. 9a, b).

4. DISCUSSION

In this section we discuss the implications of the model derived to determine the complete orientation of intragranular boundaries. In combination with the results from the example (Figs 6 -

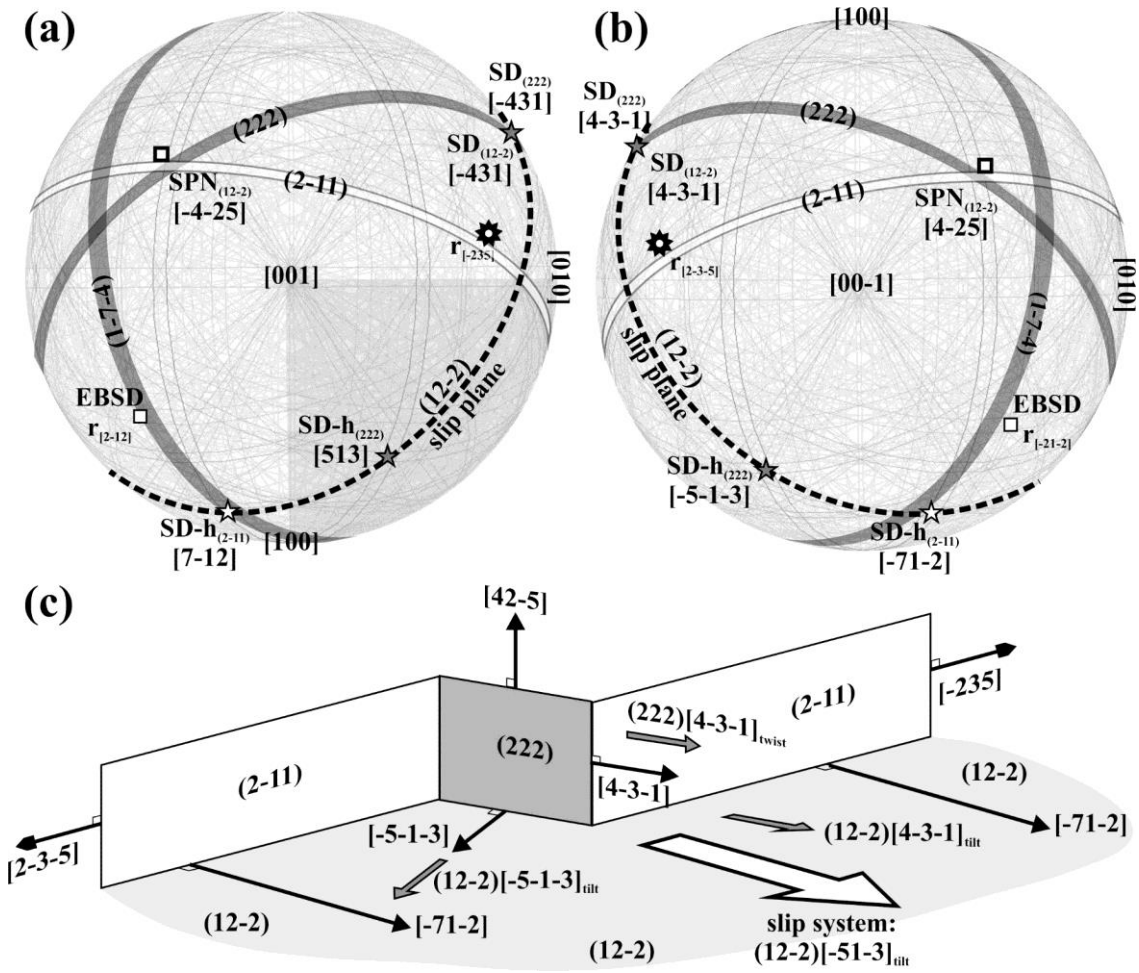

Figure 9. (a) Upper and (b) lower hemisphere SKM orthorhombic projections of the olivine intragranular boundary parameters determined by the method developed in this contribution. Also indicated are predicted crystal slip plane and directions for boundary formation as well as the misorientation axis determined by conventional EBSD analysis. (c) Schematic representation of olivine tilt and general boundary configuration and associated crystal planes, directions and slip systems.

8), we consider: (1) intragranular boundary formation and crystal slip system determination; (2) conventional (i.e. EBSD-based) misorientation analysis; (3) adapting the EC-based method for EBSD analysis; and (4) the applicability of the method for intergranular boundaries. To assist in this discussion, we have summarised Table 1 in Table 2 to compare the olivine five-parameter boundary definitions (Figs 6 - 8) with slip system determination and EBSD misorientation analysis.

4.1 Intragranular boundary formation – slip systems

The long, straight and short, kinked segments shown in Fig. 6a are clearly part of the same olivine

Table 2. Comparison of olivine five-parameter boundary definitions (Figs 6 -8), including slip systems, with EBSD misorientation analysis

	Five parameter definition					Slip system		EBSD misorientation	
Boundary	**h(hkl)**	**h[uvw]**	**ω**	**r**	**TTC**	**SP**	**SD**	**ω**	**r**
Long, straight	$(2\bar{1}1)$	$[7\bar{1}2]$	3.3°	$[2\bar{3}\bar{5}]$	0.17	$(12\bar{2})$	$[\bar{7}1\bar{2}]$	6.13°	$[2\bar{1}2]$,
Short, kinked	(222)	[513]	2.6°	$[2\bar{3}\bar{5}]$	0.45	$(12\bar{2})$ $(12\bar{2})$ (222)	$[\bar{5}1\bar{3}]$ $[4\bar{3}\bar{1}]$ $[4\bar{3}\bar{1}]$		

intragranular boundary. They share the same boundary rotation axis of $[2\bar{3}\bar{5}]$ in spite of their different boundary plane orientations, which are parallel to $(2\bar{1}1)$ and (222) respectively (Fig. 9c). However, the former is close to a pure tilt boundary (TTC = 0.17), whilst the latter is a general boundary (TTC = 0.45). The segments also differ in terms of their rotation angles, which is larger for the long, straight segment (i.e. 3.3° compared with 2.6°). This suggests that the long, straight segment represents the principal boundary and that the short, kinked segment is a minor component that may well have been removed with further boundary evolution.

In terms of intragranular boundary formation, we have assumed the standard Reed and Shockley (1950) dislocation model. Pure tilt boundaries, such as $(2\bar{1}1)$, form parallel to the boundary rotation axis and normal to the slip plane and slip direction. The slip direction is therefore normal to the boundary plane (Fig. 9c). From Eqn. 10, the boundary plane normal is determined to be $[7\bar{1}2]$, such that the slip system responsible for boundary formation is $(122)[\bar{7}1\bar{2}]$. In contrast, the normal to the (222) short, kinked boundary plane is parallel to $[\bar{5}1\bar{3}]$ suggesting slip on $(12\bar{2})[\bar{5}1\bar{3}]$ was involved in its formation. However, this is a general boundary, which require at least two slip systems to form; thus, $(12\bar{2})[\bar{5}1\bar{3}]$ can be regarded as the tilt component. For pure twist boundaries, the slip plane is parallel to the boundary plane, which is (222). The slip plane also contains the slip direction, although its precise orientation is not directly defined. We suggest that the twist slip direction is parallel to the intersection of the tilt boundary and the slip plane for the pure twist boundary, which is $[4\bar{3}\bar{1}]$ (Fig. 9a, b). Thus, the twist component of the general boundary was accommodated by slip on $(222)[4\bar{3}\bar{1}]$ (see Fig. 9c). Incidentally, the normal to the $(12\bar{2})$ slip plane

389 is $[42\bar{5}]$, which is parallel to the intersection of the two boundary segment planes (Fig. 9).
390 Consequently, the four slip systems either share or intersect with the same slip plane,
391 namely $(12\bar{2})$.

392 **4.2 Comparison with conventional (EBSD) misorientation analysis**

393 The olivine sample (Figs 6 - 8) has also been analysed via EBSD, which provides Euler angle
394 triplets for each side of the intragranular boundaries (Fig. 6b, c). EBSD software typically includes
395 misorientation analysis for specified pairs of Euler angle triplets. However, as the Euler angle
396 triplets are effectively constant for each side of the boundary, only a single pair of triplets is
397 required to determine a single misorientation angle/axis pair applicable to both long, straight and
398 short, kinked segments. The angle/axis pair determined is 6.13°/$[2\bar{1}2]$, significantly different to the
399 rotation angles and directions determined by the five parameter method (Table 2). The EBSD
400 misorientation axis $[2\bar{1}2]$ lies close to the non-displaced EC band $(1\bar{7}\bar{4})$ and is oblique to both
401 boundary segment planes/traces (Fig. 9a, b). The segments are therefore general boundaries with the
402 same characteristics according to EBSD misorientation analysis.

403 It is clear from Table 2 and Fig. 9 that conventional (EBSD) misorientation angle/axis pair analysis
404 is insensitive to boundary type and physical orientation. This is not surprising as its definition
405 recognises only the axis about which one crystal lattice needs to be rotated to bring it into alignment
406 with another (Fig. 1a); the orientation of the boundary is not involved. Thus, both segments have
407 the same misorientation angle/axis pair. The only configurations for which the misorientation axis
408 could potentially define boundary plane orientation are for pure tilt and twist boundaries; the axis is
409 parallel to the boundary plane in the former and normal to the plane in the latter. However, there
410 remain a large number of possible inclinations within either pure tilt or pure twist boundary planes
411 for a given trend (Fig. 4c, d), which makes even these ideal situations undefinable via conventional
412 misorientation analysis.

In the initial SEM/EBSD implementation of misorientation analysis (e.g. Mainprice et al., 1993; Lloyd et al., 1997), there was no requirement for two crystal lattices to be adjacent (i.e. share a common boundary), although usually the calculated misorientation 'angle/axis' pair relates to neighbouring or 'correlated' domains (Wheeler et al., 2001). Depending on crystal symmetry, there are several crystallographically related solutions for the misorientation angle/axis pair across an intragranular boundary. Convention dictates that the solution with the smallest angle is chosen, often referred to as the 'disorientation' (MacKenzie and Thomson, 1957; Hanscomb, 1958; MacKenzie, 1958; Warrington and Boon, 1975). However, an alternative approach recognises that the nearest low-index boundary axis solution defines the misorientation between adjacent lattices (e.g. Gourdet et al., 1998). The two approaches are not equivalent, which results in the distinction between coincidence site lattice (CSL) and low-order coincident axial direction (CAD) visualisations of boundary geometry (e.g. Warrington and Boon, 1975). It has been suggested (e.g. Cross and Randle, 2003) that an unambiguous analysis of intragranular boundary orientation involves consideration of the CAD solution rather than just the disorientation. The five parameter method derived in this contribution is most compatible with the CAD solution.

In fact, misorientation analysis angle/axis and five-parameter rotation angle/axis pairs are entirely different parameters. In the former they bring two crystal lattices into parallelism irrespective of whether or not the lattices share a common intragranular boundary (Fig. 1a), whereas in the latter they relate to the rotation between two originally identical crystal lattices due to the formation of an intragranular boundary (Fig. 1b-d). Thus, in misorientation analysis the misorientation axis is unconstrained by the boundary plane orientation and adopts an orientation that minimises the rotation angle between two adjacent crystal lattices. In contrast, in the five-parameter method not only is the boundary plane orientation of fundamental significance but also the dislocation model for intragranular boundary formation imposes constraints on boundary plane orientations. We suggest therefore that conventional EBSD misorientation analysis may involve ambiguity in terms of characterising intragranular boundary orientations.

4.3 Adaption to EBSD

The method developed to determine the five parameters needed to constrain the orientation of intragranular boundaries is based on observations made via SEM/EC (e.g. Figs 2d-g and 3). However, few SEM are currently capable of EC analysis and crystallographic orientation measurements are more typically made via EBSD (e.g. Fig. 2b, c). It would be useful therefore if the basic method could be adapted for EBSD-based analysis and data. A solution is provided via SKMs (e.g. Fig. 9a, b) and is illustrated using the olivine example described previously (Figs 6 - 8).

The adaption is as follows. (1) EBSD derived Euler angle triplets obtained from each side of a boundary are input into an SKM to produce maps centred on each orientation (Fig. 10a); the maps are copied into a vector drawing package. (2) Circles equivalent to ECP rocking angles (e.g. ±10°) are drawn about the centre of each map to simulate ECPs from each side of the boundary and the trace of the boundary is drawn across the centre of each pattern; 'cropping' tools are used to extract the 'ECPs' from the SKM (Fig. 10b). (3) The extracted patterns are again 'cropped' and separated along the boundary traces to form simulated 'partial ECPs' (Fig. 10c). (4) The cropped patterns are joined in appropriate pairings to simulate partial ECPs obtained by rocking about a central point on their common boundary (Fig. 10d). (5) The non-displaced EC/lattice band is identified, from which all of the parameters needed to define the complete five- parameter orientation of the boundary can be measured and/or determined via stereographic projection as per the basic method (Fig. 10e).

The adapted solutions in Fig. 10e compare favourably with the original solutions in Figs 7 and 8. They can therefore be used to determine the crystallographic orientations of the intragranular boundary planes as shown in Fig. 9. Thus, the original EC-based method devised to determine the five-parameter evolution of Intragranular boundaries can be easily adapted to EBSD data, making

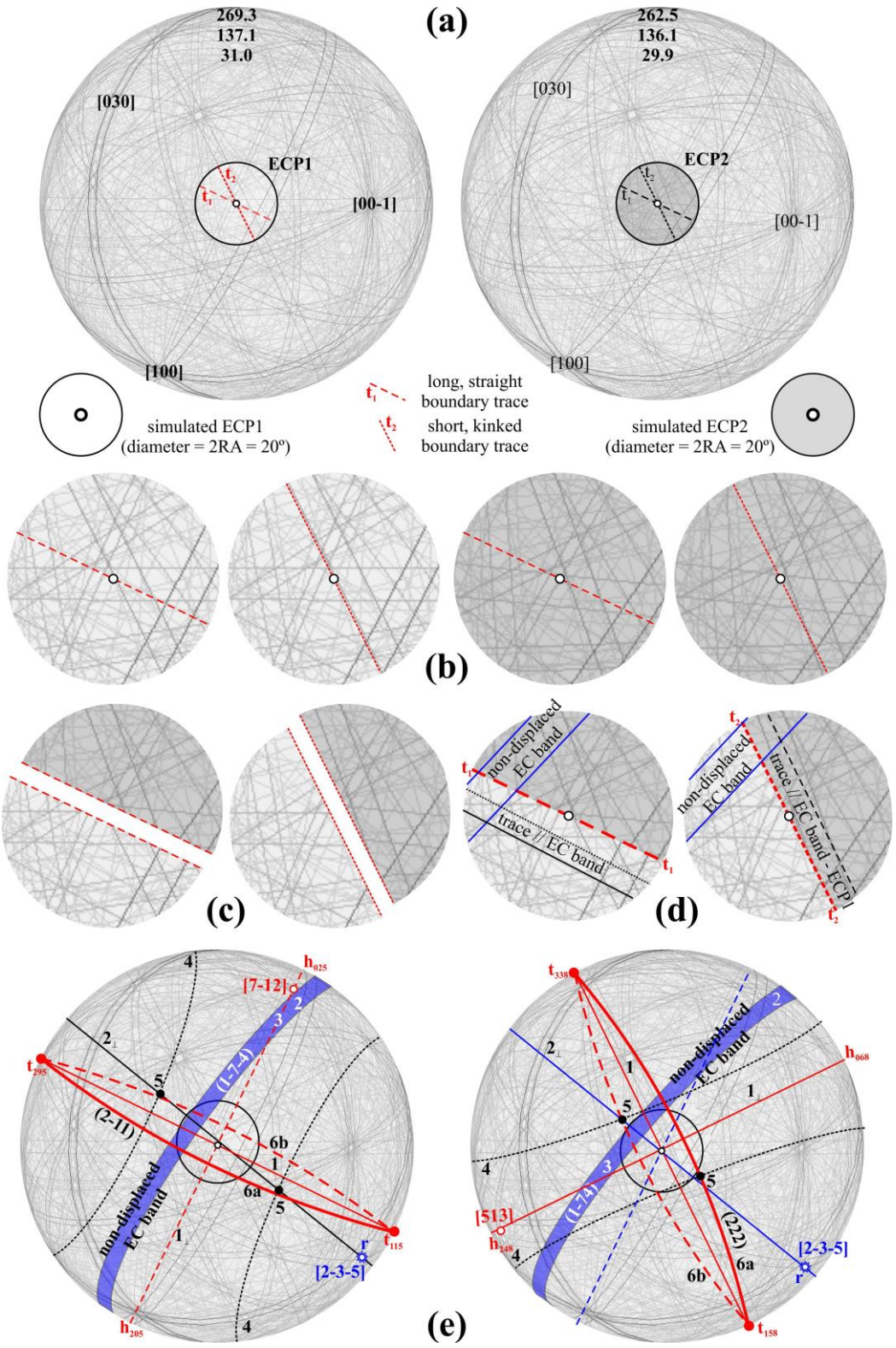

Figure 10. Adaption of the EC-based five-parameter boundary orientation method to EBSD data and analysis. Nomenclature and colours as in Figs 3 and 5. (a) *HKL Channel5*© SKMs defined by EBSD derived Euler angle triplets from each side of the olivine intragranular boundaries (Fig. 6). (b) Detail of SKM-simulated ECPs. (c) Simulated ECPs 'cropped' along boundary tracings. (d) 'Cropped' patterns joined appropriately along boundary traces to simulate partial ECPs formed by rocking about a point on the common boundary. (e) SKM representation of boundary orientation determination (1 – 6 refer to steps in the stereographic projection method, see Fig. 5): *left*, long, straight segment; *right*, short, kinked segment.

461

462 the approach more generally available.

463 **4.4 Adaption to intergranular boundaries**

464 It is generally accepted (e.g. Rohrer, 2011) that the properties and behaviours of intergranular
465 boundaries are controlled more by the physical geometry of the interfacial plane rather than
466 crystallographic misorientation. This is because as misorientation increases so does dislocation
467 density, which reduces space between neighbouring dislocations until their cores overlap such that
468 the ordered nature of the boundary begins to break down. Unlike intragranular boundaries, which
469 develop from a common initial crystal lattice by the progressive accumulation of dislocations (e.g.
470 Reed and Shockley, 1950), there is no conventional *physical* reason why crystallographic
471 relationships should exist across intergranular boundaries. In fact, the existence of such
472 relationships may have significant implications for microstructural evolution. Thus, the method
473 developed to determine the five-parameter orientation of intragranular boundaries should not
474 necessarily be expected to apply to intergranular boundaries unless extenuating circumstances
475 apply.

476 To investigate whether the method of determining the five-parameter orientation of intragranular
477 boundaries can be adapted to intergranular boundaries, we consider the boundary relationships
478 between a single olivine grain and its seven neighbouring olivine grains (Fig. 11a) in a garnet
479 lherzolite from the 90 Ma Thaba Putsoa kimberlite, Lesotho (Nixon and Boyd, 1973; Mercier and
480 Carter, 1985; Allsopp et al., 1989). The microstructure of this rock is characterised by a matrix of
481 dynamically recrystallised olivine with straight grain boundaries and frequent 120° triple junctions,
482 with a well-developed if somewhat unusual crystallographic preferred orientation (see Wallis et al.,
483 2019). EBSD data were acquired at the University of Leeds using Oxford Instruments Aztec 2.1
484 software on a FEI Quanta 650 field-emission gun SEM equipped with an Oxford Instruments
485 Nordlys-S EBSD camera. Operating conditions were: 20kV accelerating voltage, 8mm working
486 distance and 70° specimen tilt angle.

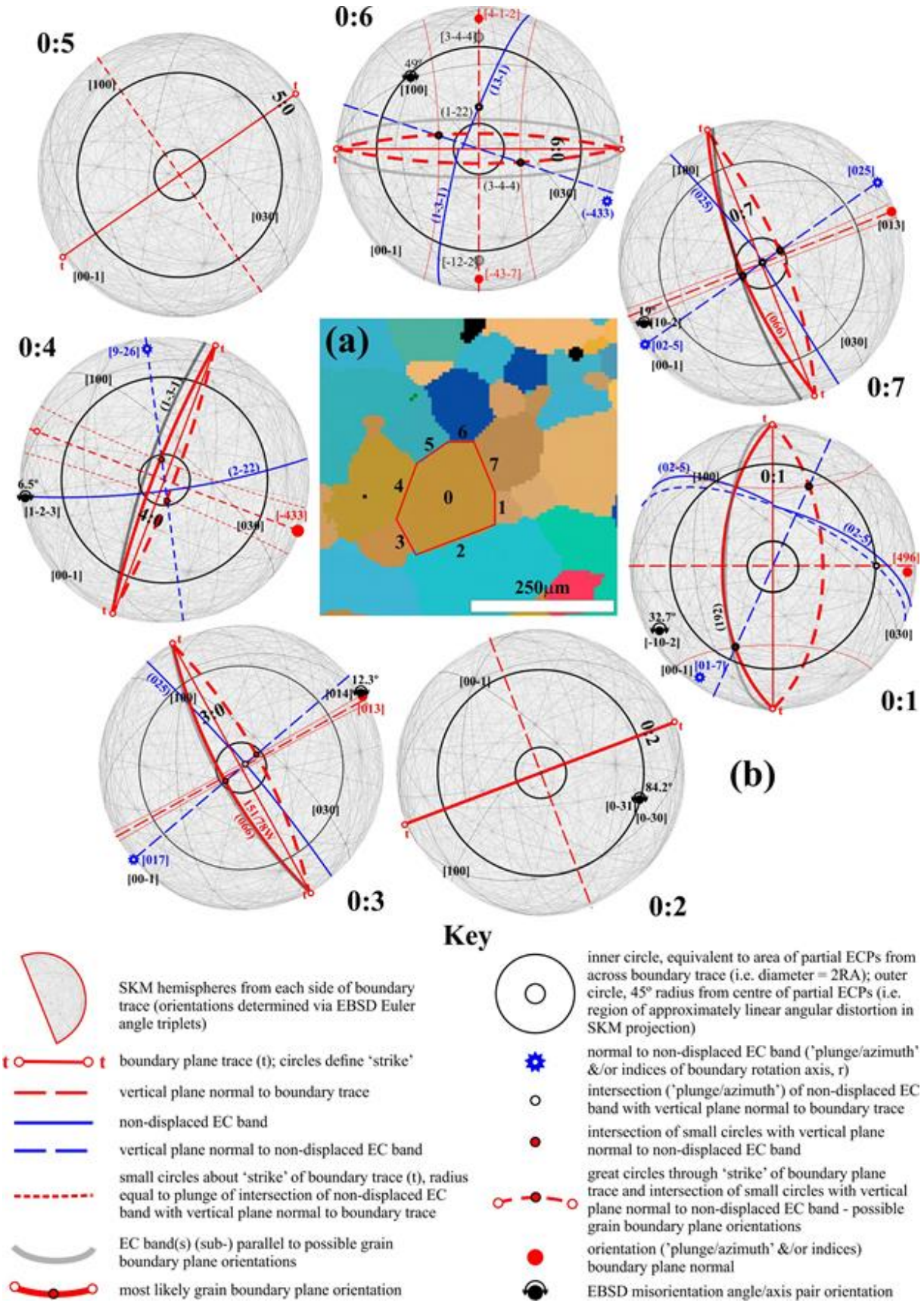

Figure 11. Example of potential adaption of method to intergranular boundary orientation determination. (a) EBSD 'all Euler' image of an olivine grain (0) and its immediate neighbours (1-7) from a garnet lherzolite, Thaba Putsoa, Lesotho. (b) SKM 'pairs' from each side of a boundary between grain 0 and grains 1-7; also shown are the elements of the five-parameter boundary method (see key). See Table 3 for a summary of results.

487

Euler angle triplets (Table 3) were measured from adjacent sides of each intragranular boundary (i.e. between grains 0 and 1, 0 and 2, etc.) and used to define SKM-pairs 'fitted' along the trace orientation of their common boundary (Fig. 11b), in a similar manner to partial-ECPs (e.g. Figs 7, 8 and 10). Note that the triplets and hence SKMs for Grain 0 are effectively constant. The combined partial-SKMs are then interrogated to identify the relevant relationships (see above) required to determine the boundary orientation (Fig. 11b). However, due to the increasing distortions that accrue with distance from the centre of the projection, it is advisable to consider only an approximately 45° radius small circle region about the centre.

Results of the analysis of the olivine intergranular boundary analysis (Fig. 11b) are summarised in Table 3. Of the seven intergranular boundaries considered, only one (boundary 0:5) provides no overall solution using the five-parameter method as no lattice plane is continuous across the boundary trace. Another (boundary 0:2) involves the juxtaposition of opposite hemispheres, again preventing an overall solution due to the absence of a non-displaced plane. A third (boundary 0:6) also involves the juxtaposition of opposite hemispheres but now the $(13\bar{1})$ and $(1\bar{3}\bar{1})$ planes are 'continuous' across the boundary and hence provide a potential solution but one involving two possible boundary plane orientations. The validity of this solution depends on whether the equivalence of different planes of the same family is appropriate in terms of the five-parameter method. The remaining four boundaries all provide tangible solutions based on the occurrence of non-displaced lattice planes across the boundary traces. Indeed, three of these boundaries (0:1, 0:3 and 0:7) involve the same non-displaced families of planes and hence rotation axes, specifically {025} and <019> respectively. The fourth boundary (0:4) has $(2\bar{2}2)$ as the non-displaced plane and $[5\bar{1}3]$ as its rotation axis.

Five-parameter analysis indicates that two of the intergranular boundaries (0:3 and 0:7) have the same orientation (Table 3), parallel to (066) and with boundary plane normal parallel to [037]. Interestingly, these boundaries are on opposite sides of the central grain (Fig. 11a). The other two

Table 3. Adaption to intergranular boundaries: summary of results (see Figs 11 and 12).

Boundary & Euler angle triplets			Non-displaced EC band	Rotation axis (r)	Rotation angles			Boundary plane (hkl)/[uvw]	TTC	EBSD angle/axis
					ω_r	ω_{tilt}	ω_{twist}			
137.6 102.6 39.5	**0:1**	147.8 110.8 72.6	$(02\bar{3})$	$[01\bar{4}]$	30.2	27.4	12.7	(192)/[253]	0.06	$32.7/[\bar{1}0\bar{2}]$
137.0 103.1 39.5	**0:2**	21.5 135.4 144.0	*different hemispheres – no solution*							$84.2/[0\bar{3}1]$
137.7 102.8 38.5	**0:3**	141.9 100.3 50.7	(025)	[019]	12.5	2.5	12.3	(066)/[037]	0.90	12.3/[014]
137.5 102.6 39.8	**0:4**	133.9 106.3 34.9	$(2\bar{2}2)$	$[5\bar{1}3]$	2.5	1.1	2.2	$(1\bar{3}\bar{1})[4\bar{3}\bar{3}]$	0.35	$6.5/[1\bar{2}\bar{3}]$
137.5 102.7 39.3	**0:5**	40.8 120.8 129.3	*different hemispheres -no solutions*							94.2/[221]
137.4 102.7 39.4	**0:6**	5.3 53.9 114.9	$(13\bar{1})$	$[43\bar{3}]$	*non-displaced EC band same family but not same plane; also different hemispheres*			$(1\bar{2}2)[4\bar{2}5]$	0.49	49/[100]
								$(3\bar{4}\bar{4})[5\bar{1}\bar{4}]]$	0.41	
			$(1\bar{3}\bar{1})$	$[4\bar{3}\bar{3}]$				$(1\bar{2}2)[4\bar{2}5]$	0.27	
								$(3\bar{4}\bar{4})[5\bar{1}\bar{4}]$	0.84	
137.2 103.1 39.4	**0:7**	133.7 97.8 56.8	(025)	[019]	26.5	5.5	25.8	(066)/[037]	0.90	$19.0/[10\bar{2}]$
			$(02\bar{5})$	$[01\bar{9}]$					0.68	

intergranular boundaries for which solutions have been found (i.e. 0:1 and 0: 4) are parallel to (192) and $(1\bar{3}\bar{1})$ planes respectively, with normal directions parallel to [253] and $[4\bar{3}\bar{3}]$, again respectively.

The rotation angles for the intergranular boundaries that provide five-parameter orientation solutions (Table 3) are derived by translating one of the partial SKMs parallel to the non-displaced EC/lattice plane until the SKM is reconstituted (Fig. 12). This is the same procedure used for the partial ECPs (e.g. Figs 7 and 8). The three boundaries sharing a <019> rotation axis exhibit increasing rotation angles from 12.5° (boundary 0:3), which is only just indicative of an intergranular boundary, through 26.5° (boundary 0:7) to 30.2° (boundary 0:1). However, according to their TTC values, boundaries 0:3 and 0:7, which also have the same orientation, are almost pure twist boundaries, whilst 0:1 is even closer to a pure tilt boundary. The other boundary (0:4) has a very small rotation angle and is in fact an intragranular boundary, which explains why it provides the most rigorous five-parameter orientation solution. As none of the boundaries are either pure tilt

or pure twist in character, the contributions of the tilt and twist components can also be readily determined by simple geometry (Fig. 12 and Table 3).

As the Euler angle triplets are known for each side of the seven boundaries (Fig. 11a and Table 3), HKL Channle5 software can be used to determine the conventional misorientation angle/axis pair for each boundary (Table 3). This approach is based only on the restoration of crystal lattices into

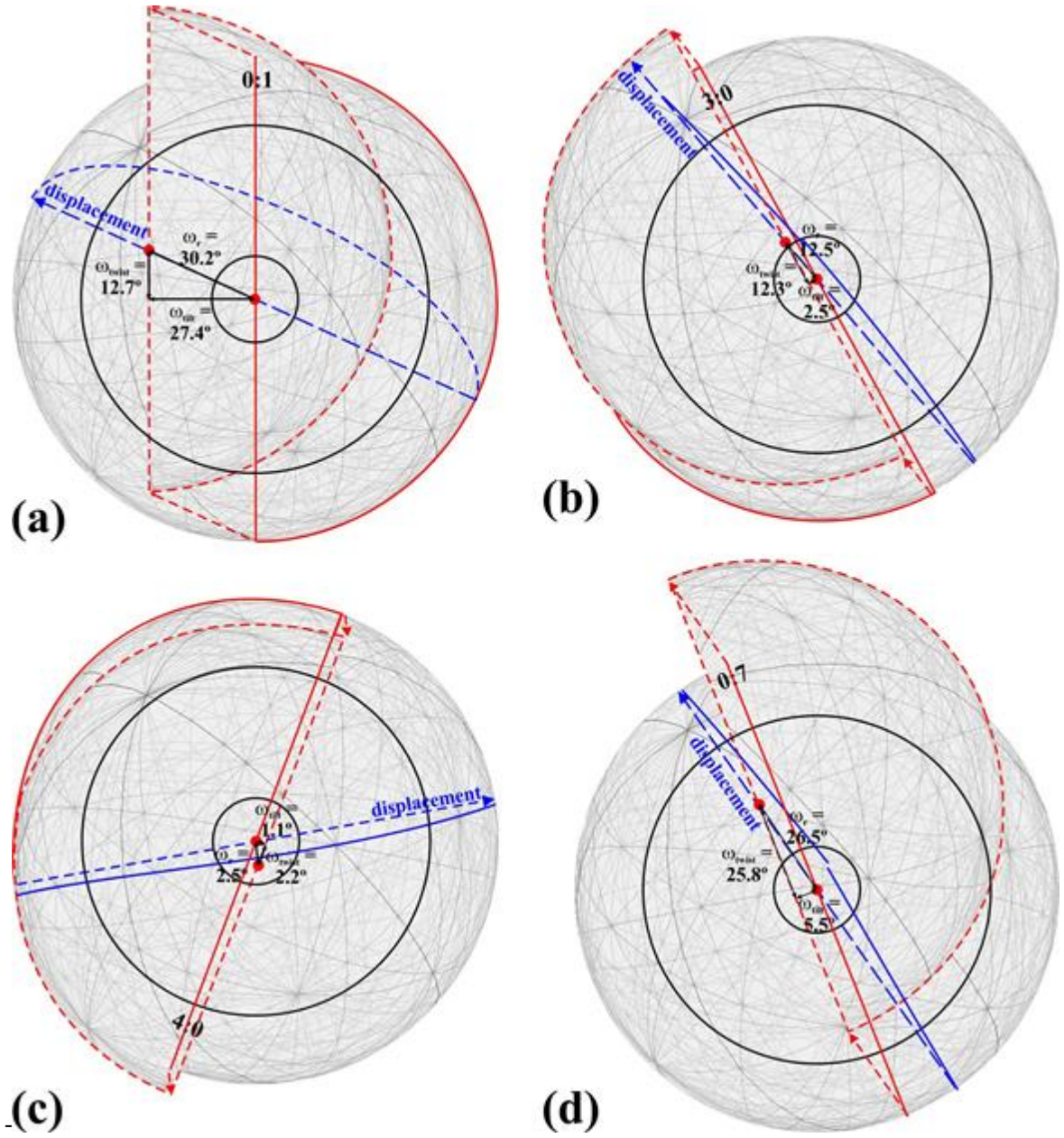

Figure 12. Determination of the total and tilt/twist component rotation angles for the four olivine inter/intra-boundaries yielding tangible five-parameter orientation solutions via translation (broken blue arrow) parallel to the non-displaced EC band (solid blue line) of one partial-SKM (broken red outline) relative to its pair until the 'disrupted' crystal lattice configuration is restored.

parallelism and takes no account of boundary orientation or configuration; thus, all seven boundaries provide a misorientation angle/axis pair. In contrast, the five-parameter method, can only provide a rotation angle/axis pair if a solution to the boundary orientation exists; that is boundaries 0:1, 0:3, 0:4 and 0:7 (see Fig. 12). A direct comparison between the two approaches is therefore only possible for these four boundaries. In general, comparisons are poor, which is not surprising as the two measures are fundamentally different. The closest match is for boundary 0:3, with the five-parameter method giving 12.5°/[019] against 12.3°/[014] for misorientation analysis. We conclude, as before for intragranular boundaries, that conventional misorientation analysis is not necessarily a good indicator of complete intergranular boundary relationships.

4.5 Related methods

Having considered how the basic method can be adapted to both EBSD data and intergranular boundaries, we can now turn to its relationship to existing methods for boundary orientation determination. Although the method presented here is new *in its entirety*, there are two existing methods that it does relate to: (1) 'plane-matching'; and (2) 'grain boundary character distribution' (GBCD).

(1) 'Plane-matching'

The 'plane-matching' method (Pumphrey, 1972) recognises that periodic lines observed in transmission electron microscope images of high angle grain boundaries result from the mismatch of either low or higher index atom planes across the grain boundary. The common factor in all observations is that there is at least one set of planes of relatively high atomic density that is either continuous or only slightly mismatched across the boundary. Watanabe (1983) and Watanabe et al. (1989) reported ECP observations of grain boundaries that they argued supported the 'plane-matching' model. This led them to suggest that ECP provided a powerful tool for the precise determination of crystallographic orientations; for example, to determine the relative orientation relationship between adjacent grains that geometrically characterise a grain boundary. In terms of

the present model, 'plane-matching' is equivalent to the non-displaced diffraction band. However, the 'plane-matching' approach does not determine the orientation of the grain boundary; rather, it constrains the direction of growth of one grain at the expense of another grain (e.g. during recrystallisation). Nevertheless, as Watanabe (1983) and Watanabe et al. (1989) provided the ECPs for the boundaries they investigated, it seems apposite to consider examples in terms of the present model, particularly as the 'plane-matching' approach did not define the boundary orientations.

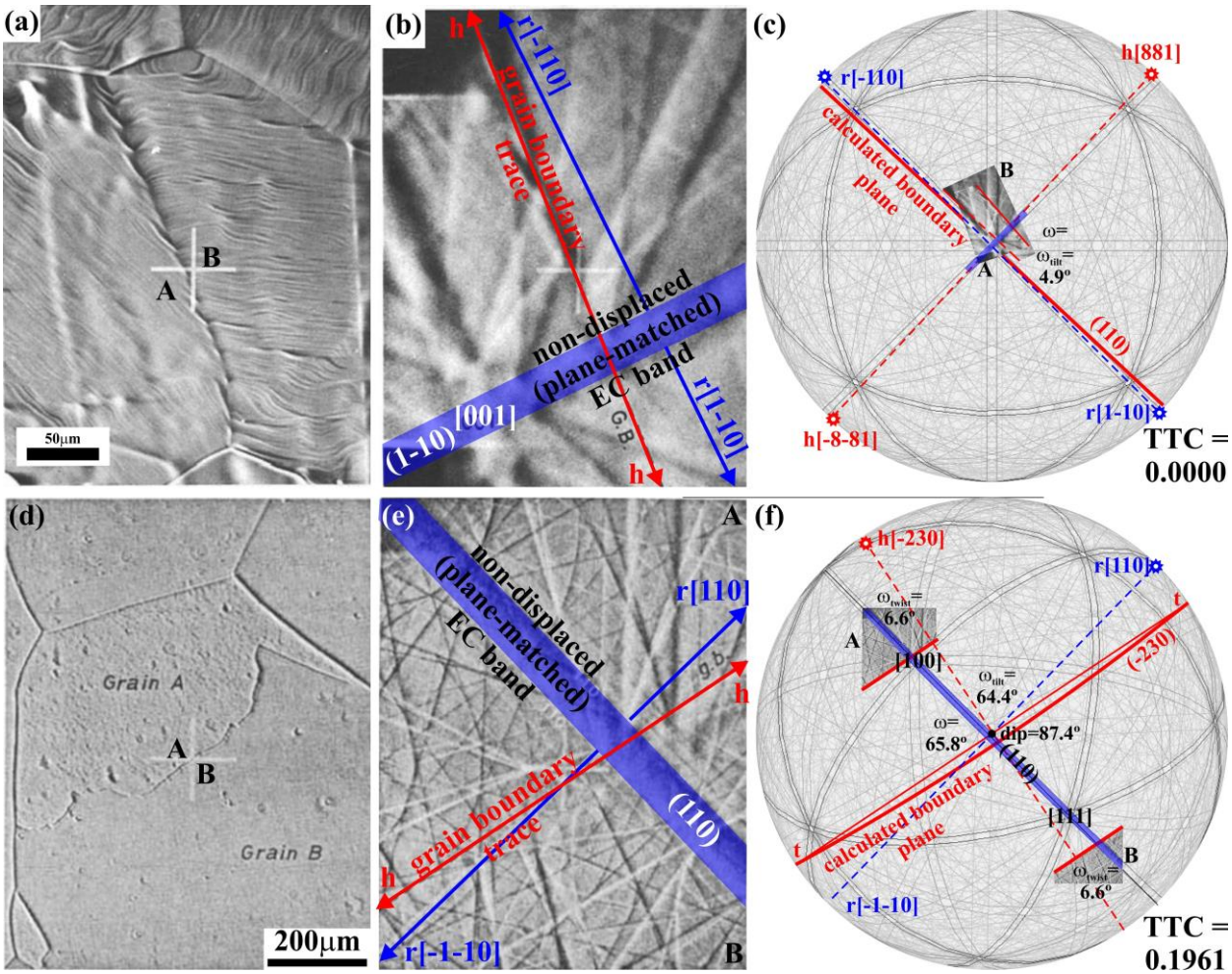

Figure 13. Comparisons between the current and 'plane-matching' methods: (a) – (c) low-angle (intragranular) boundary between two grains (A, B) in bcc Fe-6.5 mass% Si alloy (Watanabe et al., 1989, Fig. 4); (d) – (f) high-angle grain boundary between two grains (A, B) in bcc Fe-3% Si alloy (Watanabe, 1983, Fig. 1). Colour coding and nomenclature/symbols as for Figs 3, 5, 7, 8 and 10-12. (a) and (d) SEM images of boundary microstructures (cross indicates beam incident position). (b) and (e) Partial ECPs from the beam incidence positions. (e) Interpretation of the low-angle (intragranular) boundary via the current method as a vertical pure tilt boundary (TTC = 0) parallel to (110) with 4.9° misorientation. (f) Interpretation of the high-angle grain boundary via the current method as a sub-vertical (87.4° dip) general boundary (TTC = 0.20) parallel to $(\bar{2}30)$ with 65.8° misorientation comprising 64.4° tilt and 6.6° twist components.

562 The first example is a low-angle (intragranular) boundary between two grains in bcc Fe-6.5 mass%
563 Si alloy (Watanabe et al., 1989, Fig. 4; see Fig. 13a). Partial ECPs from across the boundary (Fig.
564 13b) clearly reveal the matched plane as (1-10), which is also the non-displaced EC band.
565 Superposing the partial ECPs onto a SKM for bcc iron (Fig. 13c) indicates that the matched
566 plane/non-displaced EC band passes through the projection centre; the band must therefore be
567 vertical and hence the rotation axis is horizontal, parallel to $[\bar{1}10]/[1\bar{1}0]$. Furthermore, not only
568 does the boundary trace also pass through the projection centre but it is almost coincident with the
569 vertical normal to the matched plane/ non-displaced EC band. Applying the method described in
570 this contribution constrains the boundary plane to be vertical (Fig. 13c); however, the very slight
571 off-set between boundary trace and non-displaced EC band means that the boundary plane normal
572 direction is parallel to $[881]/[\bar{8}\bar{8}1]$. Combining these directions with the rotation axes via the Excel
573 spreadsheet in the Appendix yields a TCC value of zero; thus this is a pure tilt boundary. Finally,
574 using the internal scaling present in the ECPs and SKM (Fig. 13c) allows the tilt angle to be
575 determined as 4.9°, confirming this as a low-angle (intragranular) boundary.

576 The second example is a high-angle grain boundary between two grains in bcc Fe-3% Si alloy
577 (Watanabe, 1983, Fig. 4; see Fig. 13d). Partial ECPs from across the boundary (Fig. 13e) reveal the
578 matched plane and hence non-displaced EC band to be (110). Superposing the partial ECPs onto a
579 SKM for bcc iron (Fig. 13f) indicates that the matched plane/non-displaced EC band does not quite
580 pass through the projection centre; the band therefore is not quite vertical and hence the rotation
581 axis is sub-horizontal parallel to [110]. Whilst the boundary trace almost passes through the
582 projection centre, it is clearly not parallel to the matched plane/non-displaced EC band. Applying
583 the method described in this contribution constrains the boundary plane to be parallel to $(\bar{2}30)$ and
584 to dip at 84.7°, with the boundary plane normal direction constrained to be parallel to $[\bar{2}30]$ (Fig.
585 13f). Combining these directions with the rotation axes via the Excel spreadsheet in the Appendix
586 yields a TCC value of 0.20, indicating a general boundary albeit with a dominant tilt component.
587 Using the internal scaling present in the ECPs and SKM (Fig. 13f) allows not only the total

588 boundary misorientation to be determined at 65.8° but also the tilt and twist components at 64.4°
589 and 6.6° respectively. The fact that such a large grain boundary misorientation can still exhibit a
590 matched plane/non-displaced EC band suggests that the two adjacent grains share an affinity (see
591 Watanabe et al., 1989).

592 *(2) GBCD*

593 In principal, the GBCD method (e.g. Watanabe, 1979, 1984, 1986 and 1988; Watanabe et al., 1981
594 and 1986) should have much in common with our method as it targets the five parameters needed to
595 define the complete orientation of a boundary. However, in practice there are significant differences
596 between the two approaches. GBCD concerns the description of the type and frequency of grain
597 boundaries in polycrystalline materials. In particular, it seeks to characterise the distribution of
598 special types of boundaries that might impact upon material properties and behaviours. The grain-
599 boundary distribution is expressed in terms of the conventional five parameters from measurements
600 of grain orientations and the orientations of the lines formed where grain boundaries intersect the
601 plane of observation. The fundamental aim of GBCD is to provide a quantitative description of the
602 amount and type of (special) boundaries that are present in a polycrystalline material (e.g. CSLs).

603 A significant advantage that the GBCD approach has over the method presented here is that it has
604 been automated via EBSD and stereology (e.g. Saylor and Rohrer, 2002; Saylor et al., 2004; Rohrer
605 et al., 2004b; Marquardt et al., 2015; Marquardt & Faul, 2018) and hence can consider large
606 populations of boundaries that potentially provide statistically significant observations. However,
607 the method does have disadvantages. In particular, it requires either 3D EBSD data derived via
608 serial sectioning or 2D EBSD data from samples lacking CPO to ensure the approximately random
609 distribution required for stereological determination of grain boundary normal directions (Randle
610 and Davies 2001; Rohrer 2007 and 2011; Brandon 2010; Marquardt et al., 2015). In addition,
611 GBCD relies on the three disorientation parameters to define the minimum misorientation
612 angle/axis pair, which we have suggested is independent of boundary orientation except in special

circumstances. Further comparison between GBCD and the method described here is beyond the scope of this contribution.

4.6 Accuracy, precision and error

The method introduced here is overtly manual and practical, even when involving Euler angle triplets determined via EBSD. It is therefore subject to the accuracy, precision and error limitations inherent in such approaches, particularly in terms of visual inspection/interpretation and manual measurements. In general, errors depend on the resolution and quality of the diffraction patterns (either EC or EBSD), the size of the spherical region, boundary inclination and the precision of the stereographic projection, amongst other factors. As such, it is difficult if not impossible to derive precise relative error(s) or error function(s). Nevertheless, the original potential error from which all others ultimately derive is in the recognition of the non-displaced diffraction band and the associated linear and/or angular measurements (misorientation displacements and/or angles). If the non-displaced band is clearly defined and particularly if it is located within~45° of the centre of projection, then measurements should be both accurate and precise. However, if the non-displaced band is poorly defined, which tends to be exacerbated if it occurs towards the periphery of the projection, then accuracy and indeed precision are impacted. In general, the best possible accuracy is probably to within one decimal place for both angular and linear measurements. In terms of actual boundary orientations, this means that steeper boundaries are likely to be more accurately defined than shallower boundaries.

Whilst the accuracy and precision in locating the boundary trace are typically high, the recognition of the actual boundary plane depends on stereographic projection. The projection involves plotting the non-displaced diffraction band and its vertical normal plane, as well as the boundary trace and normal. Initial errors in defining the non-displaced diffraction band can therefore be propagated. In general, the orientation of the boundary trace can be defined accurately for straight boundaries; however, curved boundaries need to be considered as linear segments, which must introduce some

error or approximation. In addition, magnification of boundary images and especially EBSD-derived 'maps' can also introduce pixilation of boundary traces, leading to lack of precision and error. The stereographic solution also provides two alternative boundary orientations, with the final choice depending on the presence/absence of a coincident (low-index) lattice plane, which may not be perfectly matched and hence could add additional error.

The method presented is based on the assumption that intragranular boundaries are constrained to low-index crystal lattice planes (i.e. the conventional Read-Shockley model), which can introduce limitations in solutions for boundary plane orientation and hence errors. Whilst the basic assumption can be geometrically established based on dislocation systems that usually operate with short Burger vectors, more general intragranular low angle or composite boundaries (e.g. those with orientation gradients that can be solved for combinations of different slip systems) can deviate from the conventional approach. Whilst this situation must be recognised, we would emphasise that although the basic premise of the method is the Read-Shockley model, the solutions derived are not necessarily low-index planes or directions (e.g. Tables 1-3). Indeed, the converse question can be posed as to how valid is the practice of 'rounding' the indices to the nearest low angle solution.

4.7 Future developments

This contribution has focussed on deriving a practical method to determine the complete (five-parameter) orientation of intragranular boundaries. Whilst such a method has been demonstrated, it certainly needs further testing via more examples, case studies and applications. These aspects represent current work in progress. In addition, as presented the method is overtly practical and hence applicable to relatively small datasets; it does not compare therefore with the opportunities provided by EBSD misorientation analysis, although as demonstrated such analysis may contain ambiguity in terms of boundary plane orientation. Nevertheless, the practical five-parameter boundary orientation method would certainly benefit from both quantification and automation. The former is also currently being investigated via several approaches involving definition of the

orientation matrix (g) in terms of crystal indices, Euler angle triplets and quaternions, although the plunge and azimuth of the boundary plane normal still have to be determined using the method proposed here. The latter requires (image) recognition of boundary traces and comparison of (quantitative) Euler angle triplet based orientations for adjacent regions across boundaries to define the necessary parameters. Hopefully, should the basic practical method prove viable, full quantification and automation will follow.

5. CONCLUSIONS

Boundaries are important features of polycrystalline materials and influence most properties, characteristics and behaviours. Accurate, reproducible and ideally rapid and efficient definition of boundary configuration is central therefore to furthering understanding polycrystalline materials. The complete definition of boundary orientation involves the misorientation between the crystal lattices of adjacent regions across the boundary and also the physical attitude of the boundary plane (e.g. the direction of the plane normal). Whilst it has become relatively easy and efficient to determine boundary misorientation (e.g. via EBSD in the SEM), definition of the boundary plane orientation has proved difficult.

This contribution has presented a practical method to determine the complete 'five-parameter' orientation of intragranular boundaries based on matching the spherical geometries of 'partial' SEM electron channelling patterns (ECPs) across boundary traces. The method assumes that intragranular boundaries are constrained to low-index crystal lattice planes (i.e. Read-Shockley model) and relies on recognising electron channelling bands, equivalent to crystal lattice planes, which are not displaced across or are parallel to the boundary trace. The former indicates the translation or displacement direction of one side of the boundary relative to the other, such that its normal direction defines the boundary rotation axis. Stereographic projection considerations of the spherical geometry relationships between the non-displaced channelling band and the boundary trace, together with the boundary trace parallel channelling bands, allow for determination of the

orientation of the boundary plane. Finally, one partial pattern is translated relative to the other parallel to the non-displaced channelling band until the undistorted ECP is restored, from which the boundary rotation angle can be measured.

Although developed from EC theory for intragranular boundaries, it has been shown how the method can be adapted relatively simply to both EBSD data (i.e. Euler angle triplets), involving the use of interactive spherical Kikuchi maps, and intergranular boundaries. However, not all intergranular boundaries may possess the necessary relationships between adjacent grains. In addition, the new method not only readily distinguishes between tilt and twist boundaries but also allows the relative contributions of these two end-member forms to the statistically more common general boundary configurations to be accurately determined and represented, both in terms of component rotation angles and also the tilt-twist component (TTC) index.

Whilst this contribution is principally concerned with the derivation of a basic method to determine accurately the complete five-parameter orientation of intra- and some inter- granular boundaries, the examples included suggest that conventional (i.e. EBSD) misorientation analysis may not necessarily provide an accurate and/or reliable representation of (intragranular) boundary configurations. Misorientation analysis is based only on matching crystal lattices via rotations about a specific axis (i.e. angle/axis pairs) and is independent of boundary configuration. We anticipate therefore that our method could potentially offer a new field of analysis based on data that are readily available and stimulate discussions on the nature and significance of (intragranular) boundaries.

Acknowledgements- This paper is dedicated to the memory of Professor Adolphe Nicolas for his seminal contributions to Earth Sciences in general and to the understanding of microstructural processes in particular. We thank Andrew Walker for numerous discussions on the methods involved. GEL also thanks Dave Mainprice for many years of discussions on all aspects of misorientation. ALL was funded by a University of Leeds teaching award and University of Tromso

713 postdoctoral fellowship. MK was supported by a postdoctoral research fellowship of the Iceland
714 Research Fund (Rannís 152726-051) and a Deutsche Forschungsgemeinschaft (DFG KA 3532/2-1)
715 standard grant. We are grateful for the help and advice offered by the Journal's editors, Philippe
716 Agard and Andrea Tommasi, and for the detailed and often perceptive comments of two anonymous
717 reviewers, all of which contributed to the final version of this paper.

718 **REFERENCES**

719 Allsopp, H., Bristow, J.W., Smith, C.B., Brown, R., Gleadow, A.J.W., Kramers, J.D. and Garvic, O.
720 1989. A summary of radiometric dating methods applicable to kimberlites and related rocks. In:
721 Ross, J.L. (Ed.), Kimberlites and Related Rocks: Their Composition, Occurrence, Origin and
722 Emplacement. Blackwell, Oxford, 349–357.

723 Amouyal, Y.; Rabkin, E.; Mishin, Y. 2005. Correlation between grain boundary energy and
724 geometry in Ni-rich NiAl. *Acta Materialia* **53**, 3795−3805.

725 Bachmann, F., Hielscher, R. and Schaeben, H. 2010. Texture analysis with MTEX—free and open
726 source software toolbox. *Solid State Phenomena* **160**, 63–68.

727 Boisen, M.B. and Gibbs G.V. 1990. Mathematical Crystallography. *Reviews in Mineralogy* **15**,
728 Mineralogical Society of America, 7276.

729 Bond, W.L. 1976. *Crystal Technology*, John Wiley & Son.

730 Bragg, W. L. 1940. Discussion. Part I. *Proceedings of the Physical Society* **52**, 54-56.

731 Brandon. D. 2010. 25 Year perspective defining grain boundaries: an historical perspective: The
732 development and limitations of coincident site lattice models. *Materials Sciences Technology* **26**,
733 762–773. doi:1 0.1179/026708310X12635619987989

734 Buranova, Y., Rosner, H., Divinski, S.V., Imlau, R. and Wilde, G. 2016. Quantitative
735 measurements of grain boundary excess volume from HAADF-STEM micrographs. *Acta*
736 *Materialia* **106**, 367-373.

737 Burgers, J. M. 1939a. Some considerations on the fields of stress connected with dislocations in a
738 regular crystal lattice I. *Proceedings of the Koninklijke Nederlandse Akademie van*

739 *Wetenschappen* 42, 293-325.
740 Burgers, J. M. 1939b. Some considerations on the fields of stress connected with dislocations in a
741 regular crystal lattice II (Solutions of the equations of elasticity for a non-isotropic substance of
742 regular crystalline symmetry). *Proceedings of the Koninklijke Nederlandse Akademie van*
743 *Wetenschappen* 42, 378-399.
744 Burgers, J. M. 1940. Geometrical considerations concerning the structural irregularities to be
745 assumed in a crystal: Proceedings of the Physical Society 52, 23-33
746 Cross, I. and Randle, R. 2003. Lowest angle solution versus low-index axis solution for
747 misorientations. *Scripta Materialia* **48**, 1587–1591.
748 Dash, M.K., Karthikeyan, T. and Saroja, S. 2017. Five-parameter grain boundary determination in
749 annealed ferrite structure using electron backscatter diffraction and serial sectioning technique.
750 *Transactions of the Indian Institute of Metallurgy* **70**,133–143.
751 DOI 10.1007/s12666-016-0868-x
752 Day, A.P. 2008. Spherical EBSD. Journal of Microscopy 230, 472-486.
753 https://doi.org/10.1111/j.1365-2818.2008.02011.x
754 Day, A.P. 2009. Spherical Kikuchi maps and other rarities. In, Schwartz, A.J., Kumar, M., Adams,
755 B.L. and Field, D.P., Electron Backscatter Diffraction in Materials Science. Springer Nature
756 Switzerland AG.
757 Dingley, D.J. 1989. Developments in on-line crystal orientation determination. *Institute of Physics*
758 *Conference Series* **98**, 473–476.
759 Friedel, G. 1913. Sur les symétries cristallines que peut révéler la diffraction des rayons X. C.R.
760 Acad. Sci. Paris 157, 1533-1536.
761 Goldstein, J.I. and Yakowitz, H. 1975. *Practical Scanning Electron Microscopy*. Plenum, New
762 York.
763 Gourdet, S., Jonas, J.J and Montheillet, E. 1998. Minimum-angle versus low-index axis rotations
764 for representing small- and large-angle grain boundary misorientations in cubic lattices. *Journal*

765 *of Applied Crystallography* **31**, 204-211.

766 Grimmer, H., Bollmann, W. and Warrington, D. H. 1974. Coincidence-site lattices and complete
767 pattern-shift in cubic crystals. *Acta Crystallographica* **A30**, 197–207.
768 doi:10.1107/S056773947400043X

769 Handscomb D.C. 1957. On the random disorientation of two cubes. *Canadian Journal of*
770 *Mathematics* **10**, 85-.

771 Hielscher, R., Bartel, F. and Britton, T.B. 2019. Gazing at crystal balls: Electron backscatter
772 diffraction pattern analysis and cross correlation on the sphere. Ultramicroscopy 207,112836.

773 Hirsch, P.B., Howie, A. and Whelan, M.J. 1962. On the production of X-rays in thin metal foils.
774 *Philosophical Magazine* **7**, 2095-2100.

775 Jhang, J.W., Jain, T., Lin, H.K. and Lan, C. W. 2018. Possible twinning operations during
776 directional solidification of multi-crystalline silicon. Crystal Growth and Design 18, 2518-2524.

777 Joy, D.C. 1974. Electron channelling patterns in the SEM. In, Holt, D. B., Muir, M. D., Grant, P. R.
778 and Boswarva, I. M. (eds) *Quantitative Scanning Electron Microscopy*. Academic, London, 131-
779 82.

780 Joy D.C., Newbury, D.C. and Davidson, D.L. 1982. Electron channelling patterns in the scanning
781 electron microscope. *Journal of Applied Physics* **53**, R81-122. https://doi.org/10.1063/1.331668

782 Kim, C-S., Hu, Y., Rohrer, G.S. and Randle, V. 2005. Five-parameter grain boundary distribution
783 in grain boundary engineered brass. *Scripta Materialia* **52**, 633–637

784 Langdon, T.G. 2006. Grain boundary sliding revisited: Developments in sliding over four decades.
785 Journal of Materials Science 41, 597–609.

786 Lisle, R.J. and Walker, R.J. 2013. The estimation of fault slip from map data: The separation-pitch
787 diagram. Tectonophysics 583, 158–163.

788 Lloyd, G.E. 1987. Atomic number and crystallographic contrast images with the SEM: a review of
789 backscattered electron techniques. *Mineralogical Magazine* **51**, 3-19.

790 Lloyd, G.E., Farmer, A.B. and Mainprice, D. 1997. Misorientation analysis and the formation and

orientation of subgrain and grain boundaries. Tectonophysics 279, 55-78.

Lloyd, G.E. and Ferguson, C.C. 1986. A spherical electron-channelling pattern map for use in quartz petrofabric analysis. Journal of Structural Geology 8, 517–526.

Mackenzie, J.K. 1958. Second paper on statistics associated with the random disorientation of cubes. *Biometrika* **45**, 229-240.

Mackenzie, J.K. and Thomson, M.J. 1957. Some statistics associated with the random disorientation of cubes. *Biometrika* **44**, 205-210.

Marquardt, K. and Faul, U.H. 2018. The structure and composition of olivine grain boundaries: 40 years of studies, status and current developments. *Physics and Chemistry of Minerals* **45**, 139–172. https://doi.org/10.1007/s00269-017-0935-9

Marquardt K., Rohrer G. S., Morales L., Rybacki E., Marquardt H. and Lin B. 2015. The most frequent interfaces in olivine aggregates: the GBCD and its importance for grain boundary related processes. *Contributions to Mineralogy and Petrology* **170**, 40-57. https://doi.org/10.1007/s00410-015-1193-9

Mainprice, D., Lloyd, G.E. and Casey, M. 1993. Individual orientation measurements in quartz polycrystals - advantages and limitations for texture and petrophysical property determinations. Journal of Structural Geology 15, 1169-1187.

Mercier, J.-C. and Carter, N.L. 1985. Pyroxene geotherms. Journal of Geophysical Research 80, 3349–3362. https://doi .org /10 .1029 /JB080i023p03349.

Mohamed, F.A. 2011. Micrograin Superplasticity: Characteristics and Utilization. *Materials* **4**, 1194-1223; doi:10.3390/ma4071194

Nieto-Fuentes, R., Nieto-Samaniego, Á.F., Xu, S.-S. and Alaniz-Álvarez, S.A. 2014. Software for determining the true displacement of faults. Computers and Geosciences 64, 35–40.

Nixon, P.H. and Boyd, F.R. 1973. Petrogenesis of the granular and sheared ultrabasic nodule suite in kimberlites. In: Nixon, P.H. (Ed.), Lesotho Kimberlites. Cape and Transvaal Printers, 48–56.

Prior, D.J., Boyle, A.P., Brenker, F., Cheadle, M.C., Day, A., Lopez, G., Peruzzo, L., Potts, G.J.,

817 Reddy, S., Spiess, R., Timms, N.E., Trimby, P., Wheeler, J., Zetterström, L., 1999. The
818 application of electron backscatter diffraction and orientation contrast imaging in the SEM to
819 textural problems in rocks. *American Mineralogist* **84**, 1741–1759. http://dx.doi.org/10.2138/am-
820 1999-11-1204.
821 Prior, D.J., Mariani, E., Wheeler, J., 2009. EBSD in the Earth Sciences: applications, common
822 practice, and challenges. In: Schwartz, A., Kumar, M., Adams, B., Field, D. (Eds.), *Electron*
823 *Backscatter Diffraction in Materials Science*. Springer, Boston, MA, pp. 345–360.
824 http://dx.doi.org/10.1007/978-0-387-88136-2_26.
825 Pumphrey, P.H. 1972. A plane matching theory of high angle grain boundary structure. *Scripta*
826 *Metallurgica* **6**, 107-114.
827 Randle, V. 1993. *The Measurement of Grain Boundary Geometry*. Institute of Physics Publications,
828 Bristol.
829 Randle, V. 2003. *Microtexture Determination and its Application*, 2nd edn. Maney Press, London.
830 Randle, V. 2006. 'Five-parameter' analysis of grain boundary networks by electron backscatter
831 diffraction. *Journal of Microscopy* **222**, 69–75
832 Randle, V. and Davies, H. 2001. A comparison between three-dimensional and two-dimensional
833 grain boundary plane analysis. Ultramicroscopy 90, 153–162.
834 Read, W.T. and Shockley, W. 1950. Dislocation models of crystal grain boundaries. Physical
835 Review 78, 275-289.
836 Redmond, J.L. 1972. Null combination in fault interpretation. American Association of Petroleum
837 Geologists Bulletin 56, 150-166.
838 Rohrer, G.S. 2007. The distribution of grain boundary planes in polycrystals. Journal of the
839 Minerals Metals and Materials Society 59, 38–42.
840 Rohrer, G.S. 2011. Grain boundary energy anisotropy: a review. *Journal of Material Science* **46**,
841 5881–5895. DOI 10.1007/s10853-011-5677-3.
842 Rohrer, G.S. and Randle, V. 2009. Measurement of the five parameter grain boundary distribution

from planar sections. In, Schwartz, A.J., Kumar, M., Adams, B.L. and Field, D.P., Electron Backscatter Diffraction in Materials Science. Springer.

Rohrer, G.S., Saylor, D.M., El Dasher, B., Adams, B.L., Rollett, A.D. and Wynblatt, P. 2004. The distribution of internal interfaces in polycrystals. *Zeitschrift Für Metallkunde* **95**,197–214. doi: 10.3139/146.017934

Saylor, D.M. and Rohrer, G.S. 2002. Determining crystal habits from observations of planar sections. *Journal of the American Ceramics Society* **804**, 2799–2804.

Saylor, D.M., El Dasher, B.S., Adams, B.L. and Rohrer, G.S. 2004. Measuring the five-parameter grain-boundary distribution from observations of planar sections. *Metallurgical and Materials Transactions* **A35**, 1981–1989.

Shockley, W. and Read, W.T. 1949. Quantitative predictions from dislocation models of crystal grain boundaries. *Physical Review* **75**, 692-692.

Sutton, A.P. and Balluffi, R.W. 1995. *Interfaces in crystalline materials*. Oxford, UK: Oxford University Press.

Sutton, A.P., Banks, E.P. and Warwick, A.R. 2015. The five-dimensional parameter space of grain boundaries. *Proceedings of the Royal Society* **A471**, Article Number: 20150442. http://dx.doi.org/10.1098/rspa.2015.0442

Venables, J.A. and Harland, C.J. 1973. Electron backscattering patterns - a new technique for obtaining crystallographic in formation in the scanning electron microscope. *Philosophical Magazine* **27**, 1193-1200.

Wallis, D., Hansen, L.N., Tasaka, M., Kumamoto, K.M., Parsons, A.J., Lloyd, G.E., Kohlstedtf, D/L. and Wilkinson, A.J. 2019. The impact of water on slip system activity in olivine and the formation of bimodal crystallographic preferred orientations. *Earth and Planetary Science Letters* **508**, 51–61. https://doi.org/10.1016/j.epsl.2018.12.007

Warrington, D. H. and Boon, M. 1975. Ordered structures in random grain boundaries; some geometrical probabilities. *Acta Metallurgica* **23**, 599-607.

869 Warrington, D.H. and Bufalini, P. 1971. The coincidence site lattice and grain boundaries. *Scripta*
870 *Metallurgica* **5**, 771-776.
871 Watanabe, T. 1979. Misorientation dependence of grain boundary sliding in 1010 tilt zinc bi-
872 crystals. *Philosophical Magazine, Physics of Condensed Matter, Defects and Mechanical*
873 *Properties* **40**, 667–683.
874 Watanabe, T. 1983. Observations of plane-matching grain boundaries by electron channelling
875 patterns. *Philosophical Magazine* **A47**, 141-146. https://doi.org/10.1080/01418618308243114
876 Watanabe, T. 1984. An approach to grain-boundary design for strong and ductile polycrystals. *Res*
877 *Mechanica* **11**, 47-84.
878 Watanabe, T. 1986. Grain boundary design for new materials. In: *Grain Boundary Structure and*
879 *Related Phenomena*. Proceedings of JIMIS-4 (1986), Supplement to Transactions of the Japan
880 Institute of Metals, 73-82.
881 Watanabe, T. 1988. Grain-boundary design for desirable mechanical properties. *Journal de*
882 *Physique* **19**, 507-519.
883 Watanabe, T., Fujii, H., Oikawa, H. and Arai, K.I. 1989. Grain boundaries in rapidly solidified and
884 annealed Fe-6.5 mass% Si polycrystalline ribbons with high ductility. *Acta Metallurgica* **37**,
885 941-952.
886 Watanabe, T., Kawamata, Y. and Karashima, S. 1986. Grain boundary character distributions for
887 recrystallization structures in Fe-3'% Si. In: Grain Boundary Structure and Related Phenomena:
888 Proceedings of JIMIS-4 (1986), Supplement to Trans. of the Japan Institute of Metals, pp. 601-
889 607.
890 Watanabe, T., Yoshikawa, N., and Karashima, S. 1981. Grain boundary character distributions in
891 recrystallisation structures of deformed aluminium single crystals. In: *Proceedings of the Sixth*
892 *International Conference on Textures of Materials (ICOTOM-6)*, Vol. 1, Japanese Iron and Steel
893 Institute, Japan, 609-618.
894 Wheeler J, Prior D.J., Jiang Z., Spiess R., and Trimby P.W. 2001. The petrological significance of

misorientations between grains. Contributions to Mineralogy and Petrology 141.109–124.

Wheeler, J., Mariani, E., Piazolo, S., Prior, D.J., Trimby, P. and Drury, M.R. 2009. The weighted Burgers vector: a new quantity for constraining dislocation densities and types using electron backscatter diffraction on 2D sections through crystalline materials. *Journal of Microscopy* **233**, 482–494.

Wieser, P.E. Edmonds, M., Maclennan, J. and Wheeler, J. 2020. Microstructural constraints on magmatic mushes under Kīlauea Volcano, Hawai'i. *Nature Communications* **11**, 1-14 | https://doi.org/10.1038/s41467-019-13635-y

Xu, S.-S., Velasquillo-Martınez , L.G., Grajales-Nishimura, J.M., Murillo-Muneto, G. and Nieto-Samaniego, A.F. 2007. Methods for quantitatively determining fault slip using fault separation. Journal of Structural Geology 29, 1709-1720.

Xu, S.-S., Nieto-Samaniego, A.F. and Alaniz-Álvarez, S.A. 2009. Quantification of true displacement using apparent displacement along an arbitrary line on a fault plane. Tectonophysics 467, 107–118.

Yamada, E. and Sakaguchi, K. 1995. Fault-slip calculation from separations. Journal of Structural Geology 17, 1065-1070.

Zaefferer, S. and Elhami, N., 2014. Theory and application of electron channelling contrast imaging 1288 under controlled diffraction conditions. *Acta Materialia* **75**, 20-50. https://doi.org/10.1016/j.actamat.2014.04.018

Zhu, C., Kaufmann, K. and Vecchio, K. 2019. Automated reconstruction of spherical Kikuchi maps. Microscopy and Microanalysis 25, 912-923. DOI: https://doi.org/10.1017/S1431927619000710

APPENDIX:

Excel spreadsheet to assist crystallographic calculations involved in the five-parameter based determination of the orientation of intragranular boundaries

We have developed a simple Excel spreadsheet to perform the crystallographic calculations involved in the five-parameter based determination of the orientation of intragranular boundaries (see below). This Appendix explains the calculations, which are all standard crystallography relationships; all user input cells are indicated by bold red text. In general, the determination of the five-parameters involves crystal directions, [uvw], rather than planes, (hkl). The description is based on olivine; modifications for other phases and in particular crystal symmetries are indicated where necessary. Note that the calculations involve rounding, whilst some indices can be user-simplified.

0. Miller/Miller-Bravais conversions (hexagonal and trigonal lattices)

As the crystal operations involved in boundary determination assume Miller indices and notation (i.e. (hkl) or [uvw]), it is necessary to convert between these and Miller-Bravais indices applicable to hexagonal and trigonal lattices (i.e. (HKIL) or [UVTW]).

Miller-Bravais to Miller

Directions:	u = U – T	v = V – T	w = W	(A1a)
Planes:	h = H	k = K	l = L	(A1b)

Miller to Miller-Bravais

Directions:	U = (2u – v)/3	V = (2v – u)/3	T = (u + v)/3	W = w	(A1c)
Planes:	H = h	K = k	I = h + k	L = l	(A1d)

1. Input phase lattice constants

These are the physical dimensions (a, b, c) of the unit cell in a crystal lattice. The number of unique terms depends on crystal symmetry but three input values are required.

2. Input rotation axis

The five-parameter boundary orientation determination method requires the crystallographic

orientation of the rotation axis and boundary plane normal directions. The former is input here. However, the value may involve calculations in Sections 4 and/or 5.

3. Calculate normalised rotation axis

The calculation of TTC involves the normalised rotation axis (e.g. Amouyal et al., 2005; Jhang et al., 2018). Normalisation, $[\bar{u}\bar{v}\bar{w}]$is achieved via,

$$\bar{u} = u/\Sigma \qquad \bar{v} = v/\Sigma \qquad \bar{w} = w/\Sigma \tag{A2}$$

where $\Sigma = (a \times u + b \times v + c \times w)^{1/2}$.

4. Calculate normal [uvw] to plane (hkl) - orthorhombic lattices

In general, the normal direction to a crystal plane in non-cubic crystal lattices does not consist of the same indices due to the different lengths of the lattice constants, although there are symmetry-dependent exceptions. For example, in the orthorhombic olivine lattice, the normal to the plane (111) is not [111] but [413]. The main text explains how the reciprocal lattice concept can be used to solve this problem (i.e. Eqns 9 and 10).

5. Calculate plane (hkl) from two directions $\langle u_1v_1w_1\rangle$, $\langle u_2v_2w_2\rangle$,

When using Spherical Kikuchi Maps, lattice planes are not always displayed, particularly as their indices increase. Fortunately, any plane can be determined from two known directions (i.e. zone axes) through which it passes. First, the two zone axes are written twice, one beneath the other:

~~u_1~~	v_1	w_1	u_1	v_1	~~w_1~~
~~u_2~~	v_2	w_2	u_2	v_2	~~w_2~~

Next, the first and last pairs are excluded. Finally, the lattice plane is calculated from,

$$h = v_1 \times w_2 - v_2 \times w_1 \qquad k = w_1 \times u_2 - u_1 \times w_2 \qquad l = u_1 \times v_2 - v_1 \times u_2 \tag{A3}$$

6. Calculate tilt/twist component (TTC)

This is calculated simply from Eqn. 3 in the main text using the normalised rotation axis and boundary plane normal indices. The former is automatically copied into the calculation; the latter is input manually after appropriate use of sections 4 and/or 5.

Excel spreadsheet to assist calculation of five-parameter based orientation of intra/inte

Input values: BOLD RED; output values BOLD BLACK

0. Miller/Miller-Bravais Conversions (hexagonal and trigonal lattices)

Miller-Bravais to Miller

Direction	<U	V	T	W>	to	<u	v	w>
	1	**1**	**-2**	**0**		**3**	**3**	**0**
Plane	{H	K	I	L}	to	{h	k	l}
	1	**1**	**-2**	**0**		**1**	**1**	**0**

Miller to Miller-Bravais

Direction	<u	v	w>	to	<U	V	T	W>
	3	**3**	**0**		**1**	**1**	**-2**	**0**
Plane	{h	k	l}	to	{H	K	I	L}
	1	**1**	**0**		**1**	**1**	**-2**	**0**

1. Input Phase Lattice Constants - Olivine

a	b	**c**
4.756	**10.21**	**5.98**

2. Input Rotation Axis

u	**v**	**w**
0	**0**	**1**

3. Calculate Normalised Rotation Axis

Products of lattice constants and crystal direction

0.000	0.000	5.980

SQRT of squares of products = 5.980

Calculate normalised crystal direction:

0.000	0.000	1.000

4. Calculate normals [uvw] to planes (hkl) in orthorhombic lattices

Calculate reciprocal lattce except for [100], [010], [001] // ⊥ (100), (010), (001)

Lattice volume = 290.381

a* = 0.210 b* = 0.098 c* = 0.167

Conversion

u		a*.a*	0	0		h
v	=	0	b*.b*	0	•	k
w		0	0	c*.c*		l

Input plane (**hkl**)

		0.04421	0	0		**0**
	=	0	0.009593	0	•	**0**
		0	0	0.027964		**1**
		0		0		**0**
	=	0	x 100 =	0	=	**0**
		0.027964		2.796389		**3**

5. Calulate plane (hkl) containing two directions <uvw>

Input first direction <u1, v1 w1> Input second direction <u2, v2 w2>

u1	v1	w1	u2	v2	w2
1	**0**	**0**	**0**	**0**	**3**

Conversion expression

1	**0**	**0**	**1**	**0**	0
0	**0**	**3**	**0**	**0**	3

Calculate common plane

h	**k**	**l**
0	**-3**	**0**

6. Calculate tilt/twist component (tilt = 0 < TTC < 1 = twist)

Rotation axis ($A_{[uvw]}$) Grain boundary normal (B[uw])

u	v	w	θ	u	v	w	θ
0	0	1	0	**0**	**0**	**3**	**4.32**

Products of lattice parameters and axis indices

u	v	w	θ	u	v	w	θ
0.000	0.000	5.980	0.000	0.000	0.000	17.940	4.320

SQRT of squares of indices= 5.980 SQRT of squares of indices= 17.940

Calculate normalised rotation axis: Calculate normalised grain boundary normal:

$A^*_{[uvw]}$ =	0.000	0.000	1.000	**$N^*_{[uvw]}$ =**	0.000	0.000	1.000

TTC = $A^*_{[uvw]} \bullet N^*_{[uvw]}$ = 1.000